J. Fluid Mech. (1999), *vol.* 380, *pp.* 169–203. Printed in the United Kingdom

Effect of free-stream turbulence and other vortical disturbances on a laminar boundary layer

By S. J. LEIB[1]†, DAVID W. WUNDROW[1]† AND M. E. GOLDSTEIN[2]

[1]NYMA Inc., Lewis Research Center Group, Cleveland, OH 44135, USA

[2]National Aeronautics and Space Administration, Lewis Research Center, Cleveland, OH 44135, USA

(Received 23 December 1997 and in revised form 2 September 1998)

This paper is concerned with the effect of free-stream turbulence on the pre-transitional flat-plate boundary layer. It is assumed that either the turbulent Reynolds number or the downstream distance (or both) is small enough that the flow can be linearized. The dominant disturbances in the boundary layer, which are of the Klebanoff type, are governed by the linearized unsteady boundary-region equations, i.e. the linearized Navier–Stokes equations with the streamwise derivatives neglected in the viscous and pressure-gradient terms. The turbulence is represented as a superposition of vortical free-stream Fourier modes and the corresponding Fourier component solutions to the boundary-region equations are obtained numerically. The results are then superposed to compute the root mean square of the fluctuating streamwise velocity in the boundary layer produced by the actual free-stream turbulence. It is found that the disturbances computed with isotropic free-stream turbulence do not reach the levels measured in experiments. However, good quantitative agreement is obtained with the relatively low turbulent Reynolds number data of Kendall when the measured strong anisotropy of the low-frequency portion of his spectrum is accounted for. Data at higher turbulent Reynolds numbers are affected by nonlinearity, which manifests itself through the generation of small spanwise length scales. We attempt to model this within the context of the linear theory by choosing a free-stream spectrum whose energy is concentrated at larger transverse wavenumbers and achieve very good agreement with the data. The results suggest that even small deviations from pure isotropy can be an important factor in explaining the large amplitudes of the Klebanoff modes in the pre-transitional boundary layer, and also point to the importance of nonlinear effects. We discuss some additional effects that may need to be accounted for in order to obtain a complete description of the Klebanoff modes.

1. Introduction

This paper is concerned with the effects of vortical free-stream disturbances on transition to turbulence in flat-plate boundary layers. Weak free-stream turbulence in an otherwise uniform stream is probably the most important example of this type of

† Present affiliation: Dynacs Engineering Co. Inc., NASA Lewis Research Center, Cleveland, OH 44135, USA.

disturbance, and Dryden (1936) and Taylor (1939) were the first to study its effects on the flat-plate boundary layer. They showed that the resulting streamwise velocity fluctuations in the boundary layer were of very low frequency and reached amplitudes that were several times larger than those in the free stream.

Most of the early experiments were conducted at very low free-stream turbulence levels in order to confirm the existence of Tollmien–Schlichting waves, and the Dryden–Taylor observations did not receive much attention until Klebanoff carried out his 1971 experiments which is unfortunate since the free-stream turbulence level is usually quite high in both technological and naturally occurring flows. In addition to reproducing the earlier findings of Dryden (1936) and Taylor (1939), Klebanoff (1971) demonstrated that the disturbances grow more or less linearly with the boundary-layer thickness and that they are quite narrow in the spanwise direction. Klebanoff (1971) referred to these disturbances as 'breathing modes', because, as noted earlier by Taylor (1939), they appeared to correspond to a thickening and thinning of the boundary layer. Kendall (1991) renamed them Klebanoff modes, and that name seems to have taken hold even though they are not modes in the strict mathematical sense (i.e. they are not homogeneous solutions of an appropriate differential equation).

More recent experimental studies of this phenomenon were carried out by Arnal & Juillen (1978), Leventhal & Reshotko (1981), Kosorygin *et al.* (1982), Kendall (1985, 1991), Suder, O'Brien & Reshotko (1988), Blair (1992), Roach & Brierley (1992), Westin *et al.* (1994) and Watmuff (1997). Kendall (1998) reviews some of these more recent experiments. The most recent of these acknowledge the importance of carefully documenting the free-stream disturbance environment, but, as will be shown below, much remains to be done in this regard. Westin *et al.* (1994) collected results from a number of these experiments and showed that the root mean square (r.m.s.) of the streamwise velocity fluctuations usually grows in direct proportion to the square root of the distance from the leading edge of the plate, as observed by Klebanoff, but with proportionality constants that differ from experiment to experiment even when the amplitudes are normalized by the free-stream turbulence level. However, at least some of the data exhibit somewhat different growth rates and, in some cases, there is even a sudden increase in amplitude presumably signalling the onset of transition.

There have been a number of theoretical and numerical studies of the effect of small free-stream disturbances on flat-plate boundary layers, but only a few of these relate to the generation of Klebanoff modes. Crow (1966) carried out a linear analysis of the boundary-layer flow due to a small spanwise distortion of an otherwise uniform free stream. Goldstein, Leib & Cowley (1992) and Goldstein & Leib (1993) considered the nonlinear boundary-layer flow due, respectively, to steady normal and streamwise vorticity distortions to an otherwise uniform upstream flow in the limit of infinite disturbance Reynolds number. Goldstein & Wundrow (1998) reconsidered the former problem, and Wundrow & Goldstein (1998) the latter for the case where the disturbance Reynolds number is of order unity, and the nonlinear flow is governed by the boundary-region equations (Kemp 1951). Scaling of the governing equations shows that nonlinear effects become important when the scaled streamwise distance from the leading edge, $\epsilon x^*/L^*$, is order-one, where x^* is the dimensional streamwise coordinate, ϵ is a measure of the free-stream turbulence level, and L^* is its characteristic length scale. Numerical solutions of the nonlinear steady boundary-layer equations (Goldstein & Leib 1993) and the nonlinear steady boundary-region equations (Wundrow & Goldstein 1998) for a single free-stream Fourier mode show that nonlinear effects within the boundary layer produce a strong focusing along planes of maximum boundary-layer thickness, but do not significantly

affect the spanwise-averaged r.m.s. streamwise velocity fluctuations (Leib, Wundrow & Goldstein 1999) (but see § 7).

Bertolotti (1997) used the linearized parabolized stability equations to numerically compute the disturbance velocity due to steady and low-frequency free-stream modes and compared the results with the experimental data of Westin *et al.* (1994) and some recent unpublished data of Kendall. In Bertolotti's computations, however, the free-stream turbulence was represented by a single Fourier mode, whose amplitude was chosen to fit the experimental data.

The actual free-stream turbulence is, of course, broadband and therefore best represented as a superposition of Fourier modes. This superposition can only be used to advantage within the context of linear theory which provides considerable motivation for extending the range of applicability of the linear analysis as far as possible, especially since the only alternative appears to be the use of a full numerical simulation.

In the experiments of Westin *et al.* (1994), fluctuating streamwise velocity measurements were taken at distances from the leading edge ranging from 100 mm to 1 m. Since our analysis shows that the Klebanoff modes are primarily generated by the transverse free-stream velocity fluctuations, the transverse integral scale and the intensity of the transverse velocity fluctuations are the appropriate length and amplitude scales to use when estimating the importance of nonlinear effects. Using the transverse integral scale, estimated to be about 8 mm (see p. 203 of their paper), for L^* and their higher turbulence level of 1.5% shows that the $\epsilon x^*/L^*$ values of the measurement points in their experiment ranged between 0.2 and 2.0 (the broadband streamwise and transverse free-stream intensities were nearly equal in this experiment). These estimates are in sharp disagreement with those made by Bertolotti (1997), who implied that nonlinear effects occur much further downstream in the Westin *et al.* (1994) experiment. (Bertolotti seems to have based his estimates on the flow conditions in Kendall's experiments. See p. 2286 of his paper.) Our estimates suggest that, while linear theory should be able to describe the initial stages of the Klebanoff mode evolution in the Westin *et al.* (1994) experiment, nonlinear effects are likely to become important beyond the first few measurement stations.

Gulyaev *et al.* (1989) used solutions of the linearized, unsteady boundary-layer equations to describe the evolution of Klebanoff modes. They showed that the boundary-layer fluctuations are driven by two independent components of the free-stream motion: a two-dimensional component, which is relatively benign, and a three-dimensional one that exhibits significant streamwise growth and therefore provides the dominant contribution to the r.m.s. streamwise velocity fluctuations. However, as even Gulyaev *et al.* (1989) point out, the Klebanoff modes cannot actually be described by the Prandtl boundary-layer equations because most of the experimental measurements lie in a region where the spanwise length scales of these modes are of the same order as the local boundary-layer thickness.

In this paper, we carry out a systematic asymptotic analysis of the effect of free-stream turbulence and other vortical disturbances on a laminar flat-plate boundary layer. We assume that the turbulent Reynolds number is small enough so that the problem can be linearized. Our results show that the analysis of Gulyaev *et al.* (1989) applies only at very small distances from the leading edge and that most of the experimental measurements lie in a region where the Klebanoff modes are governed by the unsteady boundary-region equations, i.e. the Navier–Stokes equations with the streamwise derivatives neglected in the viscous and pressure-gradient terms (Kemp 1951). These equations are elliptic, rather than hyperbolic, in the crossflow plane –

which has a significant effect on the behaviour of the solutions. Unlike the Bertolotti (1997) analysis, the upstream and far-field boundary conditions for the boundary-region equations result from strict asymptotic matching with a realistic free-stream turbulent flow.

The study of Klebanoff modes is not only important in its own right, but also because of the ubiquitous nature of the underlying phenomena. For example, the transition process in the very low-turbulence-level experiments is known to result from the orderly amplification of nearly discrete-frequency, two-dimensional, Tollmien–Schlichting waves. These primary instabilities can eventually become large enough to support oblique secondary instabilities, which then interact nonlinearly to generate strong spanwise-variable mean flow distortions (see, for example, Goldstein & Choi 1989; Goldstein 1995) that are structurally similar to the Klebanoff modes. This is an example of how different initial states can ultimately lead to a similar final state – which is consistent with the interpretation of the turbulent flow as an attractor.

The wall-layer streaks that occur in turbulent boundary layers are another example of this phenomenon (Kline *et al.* 1967). Like the Klebanoff modes, these streaks are spanwise-variable regions of high and low streamwise velocity associated with counter-rotating streamwise vortices. It is likely that they are driven by the turbulence in the outer part of the boundary layer in much the same way that Klebanoff modes are driven by free-stream turbulence. Finally, Cantwell, Coles & Dimotakis (1978) observed elongated streamwise disturbances in the wall region below growing turbulent spots. They conjectured that these were Taylor–Görter vortices generated by the passage of the spot. An alternative explanation might be that they are driven by the turbulence within the spot in the same way as the Klebanoff modes are driven by free-stream turbulence.

The problem is formulated, and the appropriate scaling is developed, in § 2. In § 3 we consider the inviscid flow above the boundary layer. The linearized unsteady boundary-layer solution is discussed in § 4, and the linearized unsteady boundary-region solution in § 5. In § 6 we derive an expression for the streamwise velocity correlation function in the boundary layer by combining the individual Fourier-component solutions to the boundary-region equations with the upstream turbulence spectrum. The relevant computations are presented in § 7, and the results are compared with data from some of the more recent experiments. The implications of the results of the analysis and computations are discussed in § 8.

2. Formulation and scaling

We consider the flow over an infinitely-thin flat plate due to a stationary, homogeneous, grid-generated turbulence field. The relatively weak turbulence field that is imposed in most of the experiments can probably be well represented (at least on a local basis) by a purely convected perturbation, say

$$\boldsymbol{u} - \hat{\boldsymbol{\imath}} = \epsilon \boldsymbol{u}_\infty(x - t, y, z), \tag{2.1}$$

of a nominally uniform mean flow, U_∞ (see § 3 and 5 below). Here $\boldsymbol{x} = x\hat{\boldsymbol{\imath}} + y\hat{\boldsymbol{\jmath}} + z\hat{\boldsymbol{k}} = \{x_1, x_2, x_3\}$ denotes the Cartesian coordinates normalized, along with all other lengths, by the transverse integral scale of the turbulence, Λ, with x in the direction of the uniform mean flow, y normal to the plate, and z along the span. The time, t, is made dimensionless with Λ/U_∞, while the velocities and pressure are normalized with U_∞ and ρU_∞^2, respectively, where ρ is the (constant) density. The small parameter ϵ is a measure of the turbulence intensity, and the scaled turbulence velocity $\boldsymbol{u}_\infty$ must satisfy

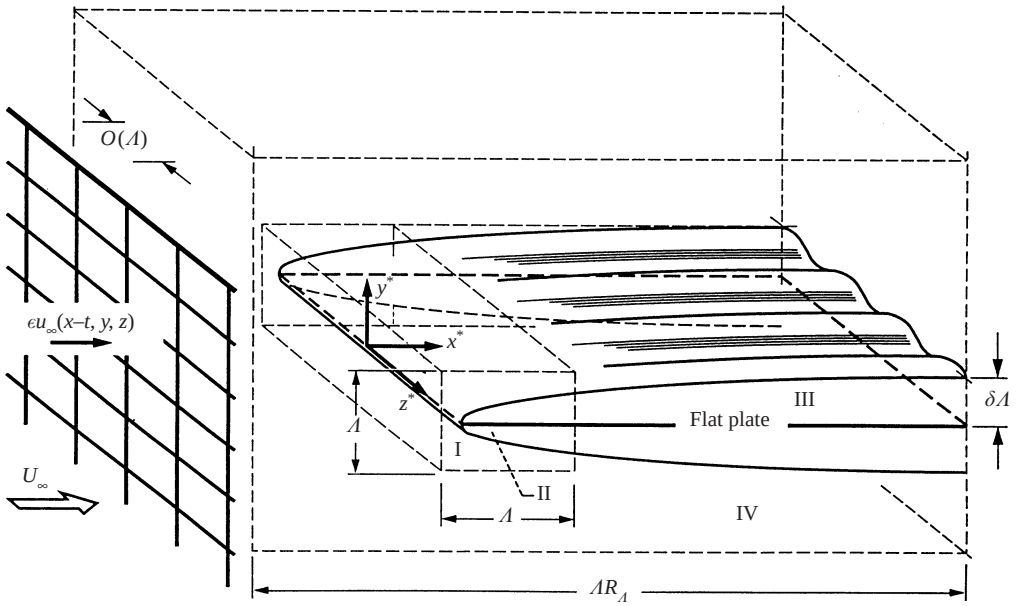

FIGURE 1. Flow configuration.

the solenoidal condition

$$\nabla \cdot \boldsymbol{u}_\infty = 0, \tag{2.2}$$

but can otherwise be specified arbitrarily as an upstream boundary condition.

Since the upstream turbulence is assumed to be stationary and homogeneous, it can be treated as a superposition of harmonic disturbances of the form

$$\boldsymbol{u}_\infty = \hat{\boldsymbol{u}}^\infty e^{i(\boldsymbol{k}\cdot\boldsymbol{x}-k_1 t)}, \tag{2.3}$$

with

$$\hat{\boldsymbol{u}}^\infty \cdot \boldsymbol{k} = 0, \tag{2.4}$$

where $\hat{\boldsymbol{u}}^\infty = \{\hat{u}_1^\infty, \hat{u}_2^\infty, \hat{u}_3^\infty\}$ and $\boldsymbol{k} = \{k_1, k_2, k_3\}$.

We suppose, at least initially, that the turbulent Reynolds number

$$r_t = \epsilon R_\Lambda, \tag{2.5}$$

is $O(1)$ where

$$R_\Lambda \equiv U_\infty \Lambda / \nu \tag{2.6}$$

is the ordinary Reynolds number based on Λ, and ν is the kinematic viscosity. This corresponds to a kind of generic scaling from which the limits $r_t \to \infty$ and $r_t \to 0$ can be obtained as special cases. Then in the asymptotic limit $\epsilon \to 0$, $R_\Lambda \to \infty$ with r_t held fixed at $O(1)$, the flow divides itself into the four asymptotic regions (Goldstein 1997) shown in figure 1.

The first of these, region I, is a primarily inviscid region of dimension $O(\Lambda)$ surrounding the leading edge, in which the motion can be treated as a linear perturbation about a uniform flow.

Beneath the linear region I is region II, where the flow is governed by the linearized

unsteady boundary-layer (LUBL) equations (Goldstein 1983; Gulyaev *et al.* 1989). However, the mean boundary-layer thickness, $\Lambda\delta$, continues to grow with x, and this solution eventually becomes invalid at the downstream distance ΛR_Λ, where $\Lambda\delta$ becomes of the order of the spanwise length scale of the unsteady boundary-layer flow, which is assumed to be of the same order as the integral scale Λ. A new solution must then be obtained when

$$x/R_\Lambda = x^*/\Lambda R_\Lambda = O(1), \tag{2.7}$$

i.e. in region III. The flow in this region is now fully three-dimensional, because the spanwise derivatives in the viscous terms are no longer negligible compared with the normal derivatives. It will be shown subsequently that the unsteady components of the motion move out of the boundary layer with increasing downstream distance, so that only the low-frequency components of the motion remain. The flow then evolves on the slow time scale

$$\bar{t} \equiv t/R_\Lambda, \tag{2.8}$$

and is governed by the unsteady boundary-region equations (Kemp 1951), which are just the Navier–Stokes equations with the streamwise derivatives neglected in the viscous and pressure-gradient terms.

Since the LUBL solution grows linearly with x, it is easy to see from (2.7) that the solution in region III can be linearized about the undisturbed, Blasius solution when

$$\epsilon R_\Lambda = r_t << 1. \tag{2.9}$$

Boundary conditions for the linearized unsteady boundary-region (LUBR) equations are obtained by requiring their solution to match with the upstream boundary-layer solution and with the outer flow above region III (i.e. the flow in region IV) where the leading-order perturbed flow is influenced by mean boundary-layer displacement effects, due to the increased boundary-layer thickness in this region.

The flow in the large outer region IV is in general nonlinear and corresponds to the usual equilibrium decay of grid-generated turbulence. It can, however, be linearized when the turbulent Reynolds number r_t is much less than one and, more generally, will behave locally like a convected perturbation of the type (2.1) over distance x_L, for which

$$x_L << 1/\epsilon = R_\Lambda/r_t, \tag{2.10}$$

which means, in effect, that it can be linearized over such distances. These order-of-magnitude estimates are somewhat optimistic in that they do not properly account for the enhanced nonlinearity that can be produced by the smaller scale components of the turbulence. They should, however, be good enough to provide adequate estimates of the overall behaviour of the flow.

Finally, we suppose that the upstream turbulence $\epsilon \boldsymbol{u}_\infty$ is specified at a distance $-x_L^\dagger$, which is large compared to unity, but small compared to R_Λ, i.e.

$$1 << -x_L^\dagger << R_\Lambda. \tag{2.11}$$

The mean flow in this region will, in general, be non-uniform, but it will vary slowly enough that the upstream boundary condition (2.1) can still be specified on a local basis independently of that flow.

3. The linear inviscid solution

The inviscid flow in region I can be determined by generalized rapid-distortion theory (Hunt 1973; Goldstein 1978). Since the problem is linear, we need only consider individual Fourier components (2.3) of the upstream distortion.

For the infinitely-thin flat plate being considered here, the flow in this region (where x and y are order one) is given by (Goldstein 1978)

$$\boldsymbol{u} = \hat{\boldsymbol{\imath}} + \cdots + \epsilon\,(\nabla\phi + \boldsymbol{u}_\infty)\,, \tag{3.1}$$

$$p = -\tfrac{1}{2} + \cdots - \epsilon\left(\frac{\partial\phi}{\partial t} + \frac{\partial\phi}{\partial x}\right), \tag{3.2}$$

where $\cdots$ represents mean boundary-layer displacement terms and, in view of (2.2), the perturbation potential ϕ is determined by Laplace's equation

$$\nabla^2\phi = 0, \tag{3.3}$$

subject to the boundary conditions

$$\phi \to 0 \quad \text{as} \quad x \to -\infty, \tag{3.4}$$

$$\phi = 0 \quad \text{at} \quad y = 0, x < 0, \tag{3.5}$$

$$\phi_y + u_{\infty 2} = 0 \quad \text{at} \quad y = 0, x > 0, \tag{3.6}$$

$$\phi \to 0 \quad \text{as} \quad y \to \infty. \tag{3.7}$$

The complete solution of the boundary-value problem (3.3)–(3.7) can be obtained using the Wiener–Hopf technique (e.g. Choudhari 1996), but our interest is in the asymptotic behaviour of the solution at large downstream distances, which can more easily be found by application of the method of variation of parameters. When the result is substituted into (3.1) and (3.2), we obtain

$$\boldsymbol{u} = \hat{\boldsymbol{\imath}} + \cdots + \epsilon\boldsymbol{u}^{(1)}\mathrm{e}^{\mathrm{i}[k_1(x-t)+k_3 z]} + \cdots, \tag{3.8}$$

$$p = -\tfrac{1}{2} + \cdots, \tag{3.9}$$

where

$$u_\sigma^{(1)}(y) = \hat{u}_\sigma^\infty \mathrm{e}^{\mathrm{i}k_2 y} + \frac{\mathrm{i}k_\sigma}{\gamma}\hat{u}_2^\infty \mathrm{e}^{-\gamma y} \quad \text{for} \quad \sigma = 1, 3, \tag{3.10}$$

$$u_2^{(1)}(y) = \hat{u}_2^\infty(\mathrm{e}^{\mathrm{i}k_2 y} - \mathrm{e}^{-\gamma y}), \tag{3.11}$$

with

$$\gamma \equiv (k_1^2 + k_3^2)^{1/2}. \tag{3.12}$$

The inviscid perturbation velocity at the surface of the plate is then given by

$$u_1^{(1)}(0) = \hat{u}_1^\infty + \frac{\mathrm{i}k_1}{\gamma}\hat{u}_2^\infty, \tag{3.13}$$

$$u_3^{(1)}(0) = \hat{u}_3^\infty + \frac{\mathrm{i}k_3}{\gamma}\hat{u}_2^\infty. \tag{3.14}$$

4. The linear boundary-layer solution

Since the mean boundary layer is of the Blasius type, the solution in region II, corresponding to the single Fourier-component inviscid solution (3.8)–(3.12), is of the form

$$\boldsymbol{u} = \left\{ F'(\eta), \left(\frac{1}{2xR_A}\right)^{1/2} (\eta F' - F), 0 \right\} + \epsilon \left\{ \bar{u}_0(\bar{x},\eta), \left(\frac{2\bar{x}k_1}{R_A}\right)^{1/2} \bar{v}_0(\bar{x},\eta), \bar{w}_0(\bar{x},\eta) \right\} \mathrm{e}^{\mathrm{i}(k_3 z - k_1 t)}, \tag{4.1}$$

with the Blasius function determined, in the usual way, by

$$F''' + FF'' = 0, \tag{4.2}$$

with $F(0) = 0$, $F'(0) = 0$, $F \to \eta - \beta$, with $\beta = 1.217\cdots$(Schlichting 1955), as $\eta \to \infty$, where

$$\eta = y \left(\frac{R_A}{2x}\right)^{1/2} = O(1), \tag{4.3}$$

and

$$\bar{x} = k_1 x, \tag{4.4}$$

is a scaled streamwise variable.

The velocity perturbation is determined by the LUBL equations

$$\left.\begin{aligned} -\mathrm{i}\bar{u}_0 + F'\frac{\partial \bar{u}_0}{\partial \bar{x}} - \frac{F}{2\bar{x}}\frac{\partial \bar{u}_0}{\partial \eta} - \frac{1}{2\bar{x}}\eta F''\bar{u}_0 + F''\bar{v}_0 &= \frac{1}{2\bar{x}}\frac{\partial^2 \bar{u}_0}{\partial \eta^2}, \\ -\mathrm{i}\bar{w}_0 + F'\frac{\partial \bar{w}_0}{\partial \bar{x}} - \frac{F}{2\bar{x}}\frac{\partial \bar{w}_0}{\partial \eta} &= \frac{1}{2\bar{x}}\frac{\partial^2 \bar{w}_0}{\partial \eta^2}, \end{aligned}\right\} \tag{4.5}$$

$$\frac{\partial \bar{u}_0}{\partial \bar{x}} - \frac{\eta}{2\bar{x}}\frac{\partial \bar{u}_0}{\partial \eta} + \frac{\partial \bar{v}_0}{\partial \eta} + \mathrm{i}\left(\frac{k_3}{k_1}\right)\bar{w}_0 = 0, \tag{4.6}$$

subject to the boundary conditions

$$\bar{u}_0 = \bar{v}_0 = \bar{w}_0 = 0 \quad \text{at} \quad \eta = 0 \tag{4.7}$$

and that $\bar{u}_0\,\mathrm{e}^{-\mathrm{i}\bar{x}}$ and $\bar{w}_0\,\mathrm{e}^{-\mathrm{i}\bar{x}}$ match onto (3.13) and (3.14) as $\eta \to \infty$.

Since k_1 and k_3 only appear as multiplicative factors in (4.6), the boundary conditions (3.13) and (3.14) suggest that we divide up the solution in the following way (Gulyaev *et al.* 1989):

$$\bar{u}_0 = \left(\hat{u}_1^\infty + \frac{\mathrm{i}k_1}{\gamma}\hat{u}_2^\infty\right)\bar{u}^{(0)} + \frac{\mathrm{i}k_3}{k_1}\left(\hat{u}_3^\infty + \frac{\mathrm{i}k_3}{\gamma}\hat{u}_2^\infty\right)\bar{u}, \tag{4.8}$$

$$\bar{v}_0 = \left(\hat{u}_1^\infty + \frac{\mathrm{i}k_1}{\gamma}\hat{u}_2^\infty\right)\bar{v}^{(0)} + \frac{\mathrm{i}k_3}{k_1}\left(\hat{u}_3^\infty + \frac{\mathrm{i}k_3}{\gamma}\hat{u}_2^\infty\right)\bar{v}, \tag{4.9}$$

and

$$\bar{w}_0 = \left(\hat{u}_3^\infty + \frac{\mathrm{i}k_3}{\gamma}\hat{u}_2^\infty\right)\bar{w}. \tag{4.10}$$

Then $\{\bar{u}, \bar{v}, \bar{w}\}$ and $\{\bar{u}^{(0)}, \bar{v}^{(0)}, 0\}$ each satisfy the momentum equations (4.5), the latter

satisfies the continuity equation (4.6), while the former satisfies

$$\frac{\partial \bar{u}}{\partial \bar{x}} - \frac{\eta}{2\bar{x}}\frac{\partial \bar{u}}{\partial \eta} + \frac{\partial \bar{v}}{\partial \eta} + \bar{w} = 0. \tag{4.11}$$

Both components satisfy the no-slip condition (4.7) at the wall, and matching with (3.13) and (3.14) requires

$$\left.\begin{array}{c} \bar{u} \to 0, \bar{w} \to \mathrm{e}^{\mathrm{i}\bar{x}} \\ \bar{u}^{(0)} \to \mathrm{e}^{\mathrm{i}\bar{x}} \end{array}\right\} \text{ as } \quad \eta \to \infty. \tag{4.12}$$

The solution of (4.5) and (4.6) (or (4.11)) must satisfy appropriate upstream boundary conditions as $\bar{x} \to 0$. The time-dependent terms, $-\mathrm{i}\bar{u}_0$ and $-\mathrm{i}\bar{w}_0$, drop out of (4.5) in this limit, and the relevant solutions are easily shown to be

$$\left.\begin{array}{l} \bar{u} \to \frac{1}{2}\bar{x}\eta F'', \quad \bar{v} \to \frac{1}{4}\left(\eta^2 F'' - 3\eta F' - F\right), \quad \bar{w} \to F' \\ \bar{u}^{(0)} \to \frac{1}{2}\left[(\eta F')' + F'\right], \quad \bar{v}^{(0)} \to \dfrac{1}{4\bar{x}}\left[\eta\,(\eta F')' - F\right] \end{array}\right\} \quad \text{as} \quad \bar{x} \to 0, \tag{4.13}$$

which shows that the streamwise velocity $\bar{u}^{(0)}$ remains bounded while $\bar{u}$ grows linearly with $\bar{x}$.

The solution in region II depends on the frequency parameter, k_1, only through the scaled streamwise variable $\bar{x}$. The limit $\bar{x} \to 0$ may therefore be interpreted as either the low-frequency limit, $k_1 \to 0$, with x fixed, or the upstream limit, $x \to 0$, with k_1 fixed. Likewise, the limit $\bar{x} \to \infty$ may be interpreted as the high-frequency limit, $k_1 \to \infty$, with x held fixed, or the downstream limit, $x \to \infty$, with k_1 fixed.

Solutions for the two-dimensional component $\left\{\bar{u}^{(0)}, \bar{v}^{(0)}, 0\right\}$ were obtained by Lighthill (1954) using an integral technique. The most recent numerical solutions for this quantity are given by Choudhari (1996). His results show that the disturbance velocity moves out of the boundary layer as $\bar{x}$ increases. Our interest here is in the three-dimensional component, $\{\bar{u}, \bar{v}, \bar{w}\}$, whose streamwise velocity initially increases linearly with $\bar{x}$ at a rate which increases with increasing spanwise wavenumber. Numerical solutions for this component are also presented by Choudhari (1996). His results show that the streamwise velocity exhibits a pronounced peak at an order-one value of η, which increases toward the boundary-layer edge as $\bar{x}$ increases, but at a slower rate than the $\left\{\bar{u}^{(0)}, \bar{v}^{(0)}, 0\right\}$ component. As noted by Choudhari (1996), this streamwise velocity profile strongly resembles that of the Klebanoff modes generated by turbulence in the free stream – even though these results correspond to a single Fourier component of the free-stream motion.

Figure 2 is a plot of the peak of the streamwise velocity perturbation magnitude, and the associated transverse position $\eta_{\max}$, as a function of $\bar{x}$ computed using a second-order, finite-difference scheme. It clearly shows the movement of the peak location toward the edge of the boundary layer with increasing $\bar{x}$. In the next subsection, we consider the asymptotic solution for the $\{\bar{u}, \bar{v}, \bar{w}\}$ component as $\bar{x} \to \infty$.

4.1. *Asymptotic solution for* $\bar{x} \to \infty$

This solution is of the WKBJ form

$$\{\bar{u}, \bar{v}, \bar{w}\} = \left\{\bar{U}(\eta, \bar{x}), \frac{\bar{V}(\eta, \bar{x})}{(2\bar{x})^{1/2}}, \bar{W}(\eta, \bar{x})\right\} \mathrm{e}^{\mathrm{i}\bar{x} - (2\bar{x})^{1/2}\Theta(\eta)}, \tag{4.14}$$

in the region where $\eta = O(1)$.

Substituting this into the LUBL equations, and taking the limit as $\bar{x} \to \infty$, shows

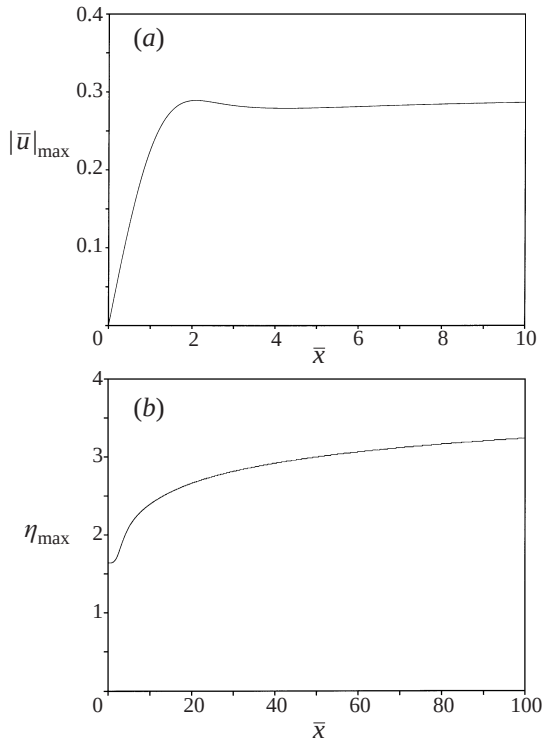

FIGURE 2. Downstream evolution of (*a*) the peak of the streamwise velocity perturbation magnitude and (*b*) it associated transverse position.

that

$$\Theta'^2 = \mathrm{i}(F' - 1), \tag{4.15}$$

at lowest approximation, and at next order that the crossflow velocity amplitude $\bar{W}$ is determined by

$$\left(F'\Theta - F\Theta'\right)\bar{W} = 2\Theta'\bar{W}' + \Theta''\bar{W}, \tag{4.16}$$

with a similar equation for $\bar{U}$.

Equation (4.16) is easily integrated to show that

$$\bar{w} = \frac{c_0(\bar{x})}{(\Theta')^{1/2}} \mathrm{e}^{H(\eta)+\mathrm{i}\bar{x}-(2\bar{x})^{1/2}\Theta}, \tag{4.17}$$

where

$$\Theta(\eta) = \mathrm{e}^{-\mathrm{i}\pi/4} \int_{\eta}^{\infty} (1 - F')^{1/2} \mathrm{d}\eta, \tag{4.18}$$

$$H \equiv \frac{1}{2}\left(\ln F'' + \int_0^{\eta} \frac{F'\Theta}{\Theta'} \mathrm{d}\eta\right), \tag{4.19}$$

and $c_0(\bar{x})$ is given by (A 11) in Appendix A, which clearly shows that $\bar{w}$ decays exponentially fast as $\bar{x} \to \infty$ provided $\Theta = O(1)$. But $\Theta \to 0$ as $\eta \to \infty$, and the WKBJ approximation therefore breaks down, i.e. it has a turning point, when

$$(2\bar{x})^{1/2}\Theta = O(1), \tag{4.20}$$

or, in view of the fact that $F \to \bar{\eta} + (A/\bar{\eta}^2)\exp(-\frac{1}{2}\bar{\eta}^2)$ as $\bar{\eta} = \eta - \beta \to \infty$, with $A = 0.331$ (Schlichting 1955), when

$$8\bar{x}A = \bar{\eta}^3 e^{\bar{\eta}^2/2}. \tag{4.21}$$

A new solution, therefore, has to be obtained in this region, which we refer to as the edge layer. The relevant expansion for this region was first proposed by Gulyaev *et al.* (1989) and is developed here in more detail in Appendix A.

While the solution (4.17) is exponentially small at $\eta = 0$, it does not vanish there. However, it can be cancelled out at this point by adding a multiple of the solution corresponding to the other root of (4.15). This amounts to replacing $\Theta(\eta)$ by

$$\Theta \to 2\Theta(0) - \Theta(\eta), \tag{4.22}$$

in (4.17), which also satisfies (4.16). The corresponding solution for $\bar{w}$ is exponentially smaller than (4.17) for all $\eta > 0$ and is therefore negligible there. A similar procedure can be used for the other velocity components. But in doing this, use has to be made of an additional exact solution discovered by Lam & Rott (1960). The result is again negligible compared with the primary solution for all $\eta > 0$.

The WKBJ solution (4.17) bears some resemblance to the large-Reynolds-number asymptotic solution of the Orr–Sommerfeld equation. However, the latter solution has its turning point near the wall, while (4.17) breaks down near the edge of the boundary layer and is therefore not connected to the Tollmien–Schlichting waves (Gulyaev *et al.* 1989).

The present analysis shows that the velocity fluctuations move out into the edge layer like $(\ln \bar{x})^{1/2}$ as $x \to \infty$ with k_1 fixed (Brown & Stewartson 1973) and that the boundary-layer fluctuations at any given x are dominated by the frequencies corresponding to $\bar{x} = k_1 x = O(1)$. The numerical results, together with the asymptotic solution, therefore suggest that the streamwise velocity fluctuations are dominated by their low-frequency components, $k_1 << 1$, at the large downstream distances where $x >> 1$. And since the actual physical solution is multiplied by the wavenumber ratio k_3/k_1, the small-spanwise-length-scale components should exhibit the most rapid growth, which is consistent with the experimental observations of Klebanoff and subsequent researchers.

Klebanoff found the spanwise wavelength to be five times larger than the boundary-layer thickness, but in most (if not all) of the more recent experiments (Kendall 1985; Westin *et al.* 1994), the spanwise wavelength was nearly equal to the boundary-layer thickness, so that the relevant solutions cannot be determined by the linearized boundary-layer equations.

5. The linear boundary-region equations

As the low-frequency, small-spanwise-length-scale components of the unsteady motion grow downstream, and the boundary-layer thickness continues to increase, the boundary-layer equations eventually become invalid. This occurs when $x = O(R_A)$ (see 2.7) and, since $\bar{x} = k_1 x$ remains order one, it implies that $k_1 R_A = O(1)$. The decomposition of the velocity components, (4.8)–(4.10), suggests that the pressure fluctuations should be of the form

$$p = -\tfrac{1}{2} + \epsilon \left\{ \mathrm{i}\kappa \left(\frac{k_1}{R_A}\right)^{1/2} \left(\hat{u}_3^{\infty} + \frac{\mathrm{i}k_3}{\gamma}\hat{u}_2^{\infty}\right)\bar{p} + \frac{k_1}{R_A}\left(\hat{u}_1^{\infty} + \frac{\mathrm{i}k_1}{\gamma}\hat{u}_2^{\infty}\right)\bar{p}^{(0)} \right\} e^{\mathrm{i}(k_3 z - k_1 t)}. \tag{5.1}$$

Introducing (5.1), along with the rest of the scalings in § 4, into the linearized Navier–Stokes equations, we find that the dominant three-dimensional component, $\{\bar{u}, \bar{v}, \bar{w}, \bar{p}\}$ is determined by

$$-\mathrm{i}\bar{u} + F'\frac{\partial \bar{u}}{\partial \bar{x}} - \frac{F}{2\bar{x}}\frac{\partial \bar{u}}{\partial \eta} - \frac{\eta F''}{2\bar{x}}\bar{u} + F''\bar{v} = \frac{1}{2\bar{x}}\frac{\partial^2 \bar{u}}{\partial \eta^2} - \kappa^2\bar{u}, \tag{5.2}$$

$$-\mathrm{i}\bar{v} + F'\frac{\partial \bar{v}}{\partial \bar{x}} - \frac{F}{2\bar{x}}\frac{\partial \bar{v}}{\partial \eta} - \frac{1}{(2\bar{x})^2}[\eta(\eta F')' - F]\bar{u} + \frac{(\eta F')'}{2\bar{x}}\bar{v} = -\frac{1}{2\bar{x}}\frac{\partial \bar{p}}{\partial \eta} + \frac{1}{2\bar{x}}\frac{\partial^2 \bar{v}}{\partial \eta^2} - \kappa^2\bar{v}, \tag{5.3}$$

$$-\mathrm{i}\bar{w} + F'\frac{\partial \bar{w}}{\partial \bar{x}} - \frac{F}{2\bar{x}}\frac{\partial \bar{w}}{\partial \eta} = \kappa^2\bar{p} + \frac{1}{2\bar{x}}\frac{\partial^2 \bar{w}}{\partial \eta^2} - \kappa^2\bar{w}, \tag{5.4}$$

$$\frac{\partial \bar{u}}{\partial \bar{x}} - \frac{\eta}{2\bar{x}}\frac{\partial \bar{u}}{\partial \eta} + \frac{\partial \bar{v}}{\partial \eta} + \bar{w} = 0, \tag{5.5}$$

in the limit $k_1, {R_A}^{-1} \to 0$ with $k_1 R_A \bar{x}, y = O(1)$, and we have put

$$\kappa \equiv k_3/(k_1 R_A)^{1/2} = O(1), \tag{5.6}$$

with $k_1 > 0$. Solutions for $k_1 < 0$ are obtained by taking complex conjugates of these results (see § 6).

Following Kemp (1951) and Davis & Rubin (1980), we refer to (5.2)–(5.5) as the linearized, unsteady boundary-region (LUBR) equations. They are simply the linearized Navier–Stokes equations with the streamwise derivatives neglected in the viscous and pressure-gradient terms and, as already shown, they correspond to a rational asymptotic limit of the Navier–Stokes equations.

These equations must be solved subject to appropriate far-field and upstream boundary conditions which, despite the similar nature of the equations, are rather more intricate than those for the boundary-layer equations. We derive the edge conditions for $\eta \to \infty$ by first considering the flow above region III (i.e. in region IV). The large-η asymptotic solution of (5.2)–(5.5) that matches with the solution in this region then provides the correct edge boundary condition. The upstream condition must now be specified over the entire region $y_0 = \eta\,(2\bar{x})^{1/2} = O(1)$, which includes the boundary-layer region $\eta = O(1)$, in order to account for the increased boundary-layer thickness in region III.

We again only need to consider a single Fourier component of the upstream distortion velocity (2.3) but, as noted in § 2, the mean boundary-layer displacement now affects the solution for the perturbed flow at leading order. In the outer region where $k_1 x, k_1 y = O(1)$, the velocity expands like

$$\boldsymbol{u} = \left\{\frac{\partial \Psi}{\partial y}, -\frac{\partial \Psi}{\partial x}, 0\right\} + \epsilon \boldsymbol{u}^{(0)} \mathrm{e}^{\mathrm{i}(k_3 z - k_1 t)} + \cdots, \tag{5.7}$$

where the mean-flow stream function, Ψ, is given to the required order of accuracy by (Van Dyke 1975, p. 136)

$$\Psi = y - \beta \mathrm{Re}\left(\frac{2(x+\mathrm{i}y)}{R_A}\right)^{1/2}, \tag{5.8}$$

where Re denotes the real part.

Then, since the pressure fluctuations vanish in this region, the perturbation velocity $\boldsymbol{u}^{(0)} = \boldsymbol{u}^{(0)}(\bar{x}, y)$ is determined by

$$\left(-\mathrm{i} + \frac{\partial}{\partial \bar{x}} - \frac{\partial \Psi}{\partial \bar{x}}\frac{\partial}{\partial y} - \frac{1}{k_1 R_\Lambda}\frac{\partial^2}{\partial y^2} + \kappa^2\right)\boldsymbol{u}^{(0)} = 0, \tag{5.9}$$

which becomes

$$\left(-\mathrm{i} + \frac{\partial}{\partial \bar{x}} - \frac{1}{k_1 R_\Lambda}\frac{\partial^2}{\partial \Psi^2} + \kappa^2\right)\boldsymbol{u}^{(0)} = O(k_1), \tag{5.10}$$

upon introducing Ψ as a new independent variable. The solution that satisfies the upstream boundary condition in (2.3) for $|k_1 y| << \left|\bar{x}_L^\dagger\right|$, as well as the continuity equation, is

$$\boldsymbol{u}^{(0)} = \hat{\boldsymbol{u}}^\infty \mathrm{e}^{\mathrm{i}(\bar{x} + \kappa_2 \Psi) - (\kappa^2 + \kappa_2^2)(\bar{x} - \bar{x}_L^\dagger)}, \tag{5.11}$$

where $\bar{x}_L^\dagger \equiv k_1 x_L^\dagger$ and

$$\kappa_2 \equiv k_2 / (k_1 R_\Lambda)^{1/2}, \tag{5.12}$$

is a scaled transverse wavenumber. It follows from (5.8) and (A 1) that

$$\Psi \to \frac{y^{(0)}}{(k_1 R_\Lambda)^{1/2}} \quad \text{as} \quad k_1 y \to 0, \bar{x} > 0, \tag{5.13}$$

and therefore that

$$\boldsymbol{u}^{(0)} \to \hat{\boldsymbol{u}}^\infty \mathrm{e}^{\mathrm{i}(\bar{x} + \kappa_2 y^{(0)}) - (\kappa^2 + \kappa_2^2)\bar{x}} \tag{5.14}$$

as region III is approached, where

$$y^{(0)} \equiv (2\bar{x})^{1/2}\,\bar{\eta}, \tag{5.15}$$

and use has been made of (2.11).

5.1. *Far-field boundary conditions*

The results of the previous section can now be used to determine the outer-edge boundary conditions for the boundary-region equations. Using the large-η form of the Blasius solution in (5.2)–(5.5), and rewriting in terms of $y^{(0)}$, yields

$$-\mathrm{i}\bar{u} + \frac{\partial \bar{u}}{\partial \bar{x}} = \frac{\partial^2 \bar{u}}{\partial y^{(0)2}} - \kappa^2 \bar{u}, \tag{5.16}$$

$$-\mathrm{i}\bar{v} + \frac{\partial \bar{v}}{\partial \bar{x}} + \frac{1}{2\bar{x}}\bar{v} - \frac{\beta}{(2\bar{x})^2}\bar{u} = \frac{-1}{(2\bar{x})^{1/2}}\frac{\partial \bar{p}}{\partial y^{(0)}} + \frac{\partial^2 \bar{v}}{\partial y^{(0)2}} - \kappa^2 \bar{v}, \tag{5.17}$$

$$-\mathrm{i}\bar{w} + \frac{\partial \bar{w}}{\partial \bar{x}} = \kappa^2 \bar{p} + \frac{\partial^2 \bar{w}}{\partial y^{(0)2}} - \kappa^2 \bar{w}, \tag{5.18}$$

$$\frac{\partial \bar{u}}{\partial \bar{x}} - \frac{\beta}{(2\bar{x})^{1/2}}\frac{\partial \bar{u}}{\partial y^{(0)}} + (2\bar{x})^{1/2}\frac{\partial \bar{v}}{\partial y^{(0)}} + \bar{w} = 0. \tag{5.19}$$

The solution to (5.16)–(5.19) that matches with the outer solution is

$$\bar{u} = 0, \tag{5.20}$$

$$\bar{v} = \frac{\mathrm{i}\mathrm{e}^{\mathrm{i}\bar{x}}}{(\kappa_2 - \mathrm{i}\,|\kappa|)\,(2\bar{x})^{1/2}}\left\{\mathrm{e}^{\mathrm{i}\kappa_2 y^{(0)} - (\kappa^2 + \kappa_2^2)\bar{x}} - \mathrm{e}^{-|\kappa| y^{(0)}}\right\} + \frac{|\kappa|\,\mathrm{e}^{\mathrm{i}\bar{x} - |\kappa| y^{(0)}}}{(2\bar{x})^{1/2}}\int_0^{\bar{x}} g(\check{x})\mathrm{e}^{-\mathrm{i}\check{x}}\mathrm{d}\check{x}, \tag{5.21}$$

$$\bar{w} = \frac{\mathrm{e}^{\mathrm{i}\bar{x}}}{\kappa_2 - \mathrm{i}\,|\kappa|}\left\{\kappa_2\,\mathrm{e}^{\mathrm{i}\kappa_2 y^{(0)} - (\kappa^2+\kappa_2^2)\bar{x}} - \mathrm{i}\,|\kappa|\,\mathrm{e}^{-|\kappa| y^{(0)}}\right\} + \kappa^2 \mathrm{e}^{\mathrm{i}\bar{x} - |\kappa| y^{(0)}} \int_0^{\bar{x}} g(\check{x})\mathrm{e}^{-\mathrm{i}\check{x}}\mathrm{d}\check{x}, \quad (5.22)$$

and

$$\bar{p} = g(\bar{x})\mathrm{e}^{-|\kappa| y^{(0)}}, \quad (5.23)$$

where we have used (2.4) with $k_1 << k_2, k_3$.

Equations (5.20)–(5.23) then provide the form of the far-field boundary conditions to be imposed on the boundary-region equations. The function $g(\bar{x})$ is, at this point, unknown, but its behaviour as $\bar{x} \to 0$ will be determined in the next subsection by matching (5.23) with the solution in region I.

5.2. *Upstream behaviour of the boundary-region solution*

Since the boundary-region problem describes the evolution of the low-frequency Fourier components downstream of the initial boundary-layer stage, it follows that the appropriate upstream matching conditions for this problem are given by the low-frequency, downstream limit of the solutions in regions I and II (i.e. the limit as $x \to \infty$ with $\bar{x} << 1$).

The solution for $\bar{x} \to 0$ with $\eta = O(1)$ can be obtained in the form of a power series as

$$\{\bar{u}, \bar{v}, \bar{w}, \bar{p}\} = \sum_{n=0}^{\infty} (2\bar{x})^{n/2} \left\{2\bar{x} U_n(\eta), V_n(\eta), W_n(\eta), \frac{1}{(2\bar{x})^{1/2}} P_n(\eta)\right\}. \quad (5.24)$$

Substituting this into the LUBR equations (5.2)–(5.5), and collecting like powers of $\bar{x}$, yields a system of ordinary differential equations for the terms in the series (5.24). The governing equations and boundary conditions for the first two terms in the series are given in Appendix B. The boundary conditions for $\eta \to \infty$ are obtained by matching (5.24) onto the limit of the solution (5.20)–(5.23) as $\bar{x} \to 0$ with $\eta = O(1)$.

We can form a composite solution from the power series (5.24), which is valid for $\bar{x} \to 0$, $\eta = O(1)$, and from (5.20)–(5.22), which are valid for $\bar{x} \to 0$, $y^{(0)} = O(1)$ (but not uniformly valid as $y^{(0)} \to \infty$), to obtain a small-$\bar{x}$ asymptotic solution to the LUBR equations that is uniformly valid over the entire region, $y^{(0)} = O(1)$. This solution can be constructed by adding (5.24) to (5.20)–(5.23) and subtracting out the 'common parts' to obtain

$$\bar{u} \to 2\bar{x} U_0 + (2\bar{x})^{3/2} U_1, \quad (5.25)$$

$$\bar{v} \to V_0 + (2\bar{x})^{1/2}\, V_1 + \frac{\mathrm{i}}{(\kappa_2 - \mathrm{i}\,|\kappa|)\,(2\bar{x})^{1/2}}\{\mathrm{e}^{\mathrm{i}\kappa_2 (2\bar{x})^{1/2}\bar{\eta}}\mathrm{e}^{-(\kappa^2+\kappa_2^2)\bar{x}} - \mathrm{e}^{-|\kappa|(2\bar{x})^{1/2}\bar{\eta}}\}$$
$$- \left(\frac{3\beta}{4} - \frac{1}{2} g_1\,|\kappa|\,(2\bar{x})^{1/2}\right)\mathrm{e}^{-|\kappa|(2\bar{x})^{1/2}\bar{\eta}} - \bar{v}_c\,, \quad (5.26)$$

$$\bar{w} \to W_0 + (2\bar{x})^{1/2}\, W_1 + \frac{1}{(\kappa_2 - \mathrm{i}\,|\kappa|)}\{\kappa_2 \mathrm{e}^{\mathrm{i}\kappa_2 (2\bar{x})^{1/2}\bar{\eta}}\mathrm{e}^{-(\kappa^2+\kappa_2^2)\bar{x}} - \mathrm{i}\,|\kappa|\,\mathrm{e}^{-|\kappa|(2\bar{x})^{1/2}\bar{\eta}}\}$$
$$- \frac{3\beta\,|\kappa|}{4}\,(2\bar{x})^{1/2}\;\mathrm{e}^{-|\kappa|(2\bar{x})^{1/2}\bar{\eta}} - \bar{w}_c, \quad (5.27)$$

as $\bar{x} \to 0$, where the constant g_1 is given by (B 15), the 'common parts', $\bar{v}_c$ and $\bar{w}_c$, are given in Appendix C, and we have retained the first two terms in the expansion (5.24).

This completes the specification of the boundary-region problem. In the next subsection, we describe the numerical method used to obtain solutions.

5.3. *Numerical solution*

A streamwise marching procedure, based on second-order central differences in η and backward differences in $\bar{x}$, was used to solve the LUBR equations. The pressure was computed on a grid staggered in the transverse direction relative to that for the velocity components.

As already mentioned, the upstream boundary conditions must now be specified over the entire region $y_0 = O(1)$, which includes the region $\eta = O(1)$. The composite solutions (5.25)–(5.27), which are uniformly valid in this region, were used as starting conditions. It was necessary to retain the first two terms in the upstream expansion as $\bar{x} \to 0$ in order to successfully start the procedure.

The edge boundary conditions (5.20)–(5.23) involve the unknown function $g(x)$, induced by the pressure in the outer region. Its behaviour as $\bar{x} \to 0$ is given by (B 11) and (B 15). For $\bar{x} = O(1)$, this function was eliminated from the edge conditions by imposing mixed boundary conditions on the transverse velocity components and the pressure. The resulting edge conditions are

$$\bar{u} \to 0, \tag{5.28}$$

$$\frac{\partial \bar{v}}{\partial \eta} + |\kappa|\,(2\bar{x})^{1/2}\,\bar{v} \to -\mathrm{e}^{\mathrm{i}(\bar{x}+\kappa_2(2\bar{x})^{1/2}\bar{\eta})}\mathrm{e}^{-(\kappa^2+\kappa_2^2)\bar{x}}, \tag{5.29}$$

$$\frac{\partial \bar{w}}{\partial \eta} + |\kappa|\,(2\bar{x})^{1/2}\,\bar{w} \to \mathrm{i}\kappa_2\,(2\bar{x})^{1/2}\,\mathrm{e}^{\mathrm{i}(\bar{x}+\kappa_2(2\bar{x})^{1/2}\bar{\eta})}\mathrm{e}^{-(\kappa^2+\kappa_2^2)\bar{x}}, \tag{5.30}$$

and

$$\frac{\partial \bar{p}}{\partial \eta} + |\kappa|\,(2\bar{x})^{1/2}\,\bar{p} \to 0, \tag{5.31}$$

as $\eta \to \infty$.

Second-order finite differences were used in these boundary conditions to obtain a block tri-diagonal linear system of equations, which was solved using a standard sparse system algorithm.

Figure 3 shows profiles of the magnitudes of the streamwise and spanwise perturbation velocity profiles at various values of $\bar{x}$ computed from the LUBR equations with $\kappa = 1$, $\kappa_2 = -1$. The streamwise velocity profiles look similar to the corresponding LUBL profiles (Choudhari 1996), but the strong spanwise ellipticity effects cause the peak level, which initially increases linearly with $\bar{x}$, to rapidly decrease to zero. The spanwise velocity profiles are quite different from the LUBL profiles (cf. Choudhari 1996, figure 3*b*) due to the free-stream matching requirements of (5.30).

The initial linear growth and subsequent decrease of the peak in the streamwise perturbation velocity profile is more clearly shown in figure 4, which is a plot of $|\bar{u}|$ as a function of $\bar{x}$ at $\eta = 1.64$, where the peak in the profiles occurs.

Results from additional computations show that the peak of the $|\bar{u}|$ profiles reaches a maximum and then decreases to zero very rapidly for larger values of κ and (absolute value of) κ_2; at smaller values, the initial growth and ultimate decay are much more gradual.

The LUBR equations possess an asymptotic solution of the form

$$\bar{u} = \frac{1}{\kappa^2}\hat{u}\left(\kappa^2\bar{x}, \eta; \frac{\kappa_2}{\kappa}\right), \tag{5.32}$$

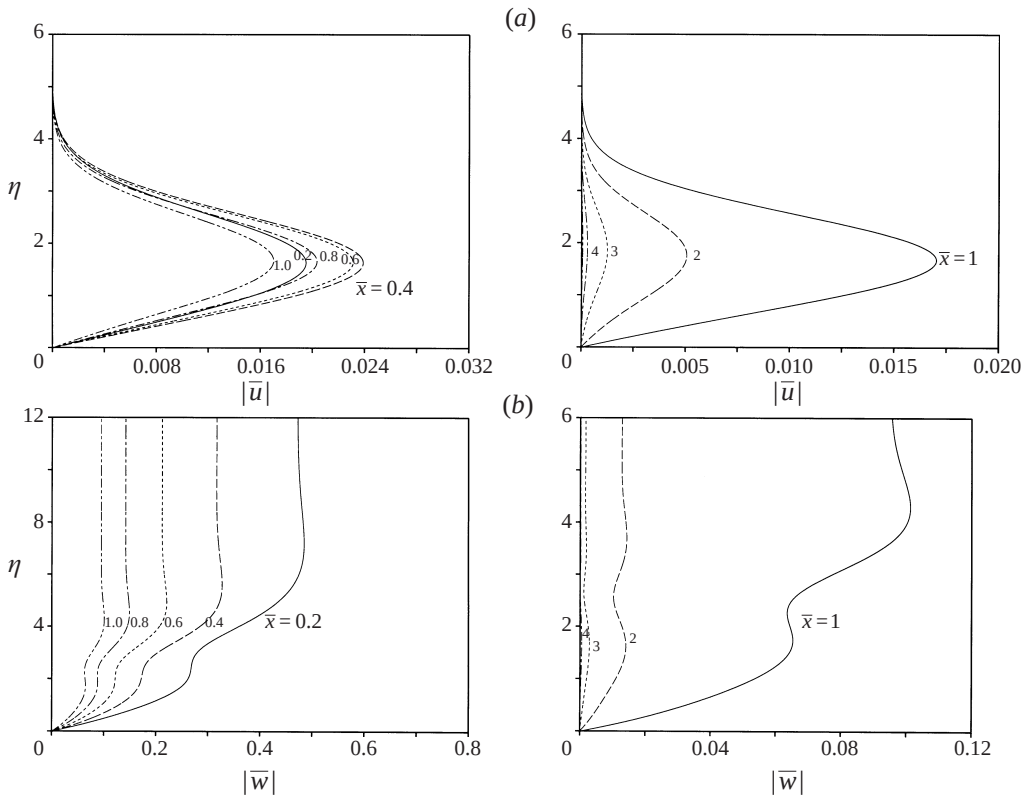

FIGURE 3. Profiles of (*a*) streamwise and (*b*) spanwise perturbation velocity at the indicated values of $\bar{x}$.

$$\bar{v} = \hat{v}\left(\kappa^2\bar{x}, \eta; \frac{\kappa_2}{\kappa}\right), \tag{5.33}$$

$$\bar{w} = \hat{w}\left(\kappa^2\bar{x}, \eta; \frac{\kappa_2}{\kappa}\right), \tag{5.34}$$

in the limit as $\kappa \to \infty$ with $\kappa_2/\kappa = O(1)$, where $\hat{u}, \hat{v}$, and $\hat{w}$ are now determined by the linearized *steady* boundary-region equations.

Figure 5(*a*) is a plot of $\kappa^2\bar{u}$ vs. $\kappa^2\bar{x}$ at fixed $\kappa_2/\kappa = -1$, $\eta = 1.64$ for various values of $\kappa \geqslant 1$. These results clearly collapse on a single curve for $\kappa \geqslant 2$, and even the $\kappa = 1$ result is not too far from this curve. In figure 5(*b*), we have plotted the same results vs. $\kappa\bar{x}^{1/2}$. Notice that, except for a small region near the origin, the steady solution increases linearly with $\kappa\bar{x}^{1/2}$ (and therefore with the boundary-layer thickness) up to $\kappa\bar{x}^{1/2}$ of about 0.5. This might lead one to suppose that the Klebanoff modes can be represented as a single steady mode (Bertolotti 1997), but, as we shall see, the unsteady (but low-frequency) solutions make the dominant contribution to the r.m.s. of the streamwise velocity fluctuations in the boundary layer.

On the other hand, the LUBR equations reduce to the LUBL equations in the limit as $\kappa \to 0$. Figure 6 shows plots of $|\bar{u}|$ vs. $\bar{x}$ at fixed $\kappa_2/\kappa = -1$, and η again equal to 1.64, at various values of $\kappa \leqslant 0.1$. The dashed curve denotes the solution calculated from the LUBL equations. The results show that solutions to the LUBR equations approach the LUBL results very slowly as $\kappa \to 0$ so that the LUBL solution used

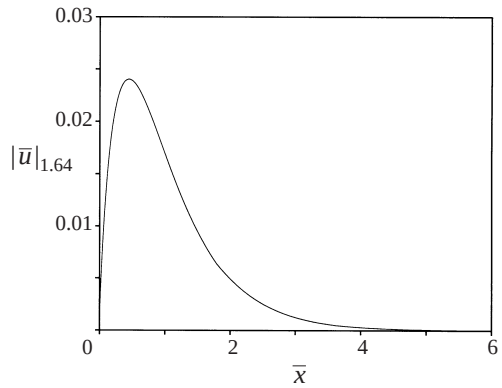

FIGURE 4. Evolution of the boundary-region streamwise velocity perturbation magnitude at $\eta = 1.64$ for $\kappa = 1, \kappa_2 = -1$.

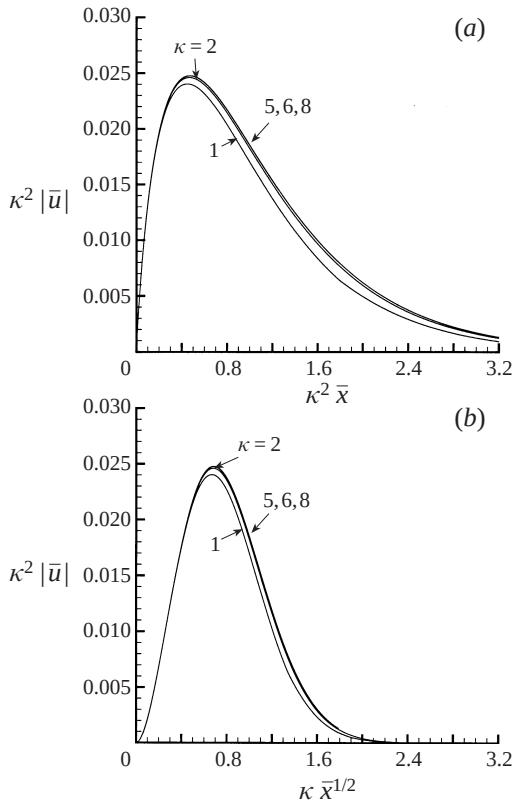

FIGURE 5. Plot of $\kappa^2|\bar{u}|$ vs. (*a*) $\kappa^2\bar{x}$ and (*b*) $\kappa\bar{x}^{1/2}$ for various values of $\kappa = -\kappa_2 \geqslant 1$.

by Gulyaev *et al.* (1989) to calculate the streamwise velocity fluctuations is only valid for very small spanwise wavenumbers. This shows that the full LUBR solutions must be used to describe the experimental results in which the spanwise wavelength is invariably of the order of the boundary-layer thickness.

Figure 7 is a plot of profiles of the normalized streamwise velocity perturbation $|\bar{u}|/|\bar{u}|_{\max}$ for various values of $\bar{x}$, with $\kappa = 1$, $\kappa_2 = -1$. The dashed curve is the mode

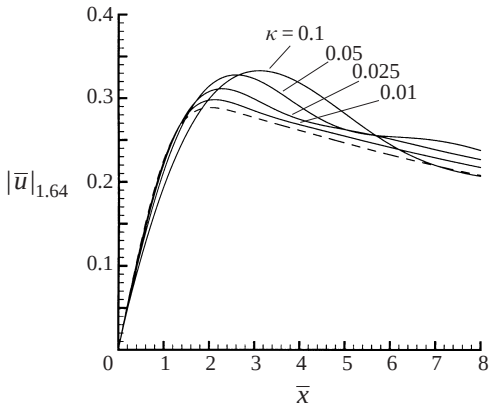

FIGURE 6. Curves of $|\bar{u}|$ at $\eta = 1.64$ vs. $\bar{x}$ for various $\kappa \leqslant 0.1$ with $\kappa_2 = -\kappa$ from the boundary region equations. The dashed curve is the corresponding boundary-layer solution.

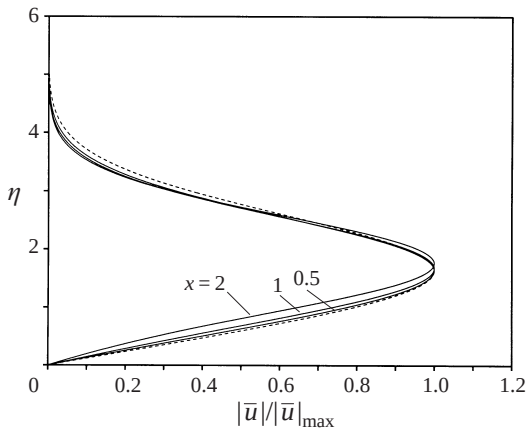

FIGURE 7. Profiles of $|\bar{u}|/|\bar{u}|_{max}$ at indicated $\bar{x}, \kappa = 1$ and $\kappa_2 = -1$. The dashed curve corresponds to $\eta F''/(\eta F'')_{1.64}$.

shape $\eta F''$, normalized by its peak value, that appears in the upstream boundary condition (4.13). This is the mode shape originally used by Taylor (1939), and later by Klebanoff (1971), to fit their experimental data. The profiles from the LUBR solution clearly come quite close to collapsing on this mode shape.

In the next section, we derive an expression for the mean-square streamwise velocity perturbation due to a broadband turbulent flow by superposing the individual Fourier component LUBR solutions.

6. Statistical quantities in the boundary layer

An important advantage of the linear analysis is that the individual Fourier-component solutions can be superposed to evaluate the statistical quantities of interest in terms of the upstream turbulence field. The decomposition (4.8)–(4.10) provides the relevant 'transfer functions' which relate the fluctuating velocity within the boundary layer to the Fourier coefficients of the upstream turbulence (Hunt 1973; Goldstein & Durbin 1980).

The quantity of most interest is the two-point, time-delayed, streamwise velocity correlation

$$R_{11}(\tau,\zeta) \equiv \langle u'(\boldsymbol{x}+\hat{\boldsymbol{k}}\zeta, t+\tau)u'(\boldsymbol{x},t)\rangle, \tag{6.1}$$

where $\epsilon u' \equiv u - F'(\eta)$ and $\langle\ \rangle$ denotes the expectation value. Then, in view of (4.8),

$$R_{11}(\tau,\varsigma) = \iiint_{-\infty}^{\infty} \mathrm{e}^{\mathrm{i}(k_3\varsigma - k_1\tau)} m^*_\ell(x,y,\boldsymbol{k}) m_m(x,y,\boldsymbol{k}) \Phi_{\infty\ell m}(\boldsymbol{k})\mathrm{d}\boldsymbol{k}, \tag{6.2}$$

where $\Phi_{\infty\ell m}$ is the upstream turbulence spectral tensor (see Batchelor & Proudman 1954; Hunt 1973), repeated indices are summed, the * denotes complex conjugation and, in general,

$$m_1 = \bar{u}^{(0)}; \quad m_2 = \frac{\mathrm{i}k_1}{\gamma}\bar{u}^{(0)} - \frac{k_3^2}{k_1\gamma}\bar{u}; \quad m_3 = \frac{\mathrm{i}k_3}{k_1}\bar{u}, \tag{6.3}$$

where γ is defined by (3.12).

The simplest upstream spectral tensor is probably the one corresponding to isotropic turbulence, namely

$$\Phi_{\infty ij} = \frac{E(k)}{4\pi k^4}(k^2\delta_{ij} - k_i k_j), \tag{6.4}$$

where $E(k)$ is the three-dimensional spectrum function, δ_{ij} denotes the Kronecker delta, and $k = \left(k_1^2 + k_2^2 + k_3^2\right)^{1/2}$. However, it is very difficult to generate truly isotropic turbulence in a laboratory experiment, and Batchelor (1946, 1953) and Chandrasekhar (1950) proposed a less restrictive, axisymmetric turbulence model (see also Lindborg 1995). Using the results of Appendix D, the corresponding spectral tensor can be written as

$$\begin{aligned}\Phi_{\infty ij} = {} & \frac{1}{k_\perp^2}\left(\Phi_t - \frac{2k_1^2}{k_\perp^2}\Phi_1\right)(k_\perp^2\delta_{ij}^\perp - k_{\perp i}k_{\perp j}) \\ & + \frac{1}{k_\perp^2}\Phi_1(k_1^2\delta_{ij}^\perp - k_1 k_{\perp i}\delta_{j1} - k_1 k_{\perp j}\delta_{i1} + k_\perp^2\delta_{i1}\delta_{j1}),\end{aligned} \tag{6.5}$$

where

$$k_{\perp i} \equiv k_i - \delta_{i1}k_1, \tag{6.6}$$

are the cross-stream wavenumber components,

$$\delta_{ij}^\perp \equiv \delta_{ij} - \delta_{i1}\delta_{j1}, \tag{6.7}$$

is the cross-stream Kronecker delta, $k_\perp = \left(k_2^2 + k_3^2\right)^{1/2}$, and the scalars $\Phi_1(k_1,k_\perp)$ and $\Phi_t(k_1,k_\perp)$ are related to the longitudinal and lateral one-dimensional spectrum functions, $E_1(k_1)$ and $E_t(k_1)$, respectively, by

$$E_1(k_1) = 2\pi\int_0^\infty \Phi_1 k_\perp \mathrm{d}k_\perp, \tag{6.8}$$

and

$$E_t(k_1) = 2\pi\int_0^\infty \Phi_t\, k_\perp \mathrm{d}k_\perp. \tag{6.9}$$

For isotropic turbulence $\Phi_t - 2(k_1/k_\perp)^2\Phi_1 = \Phi_1 = k_\perp^2 E/4\pi k^4$, and (6.5) reduces to (6.4).

The contribution of $\bar{u}^{(0)}$ to the integral in (6.2) is smaller than that of $\bar{u}$ by a factor

of $(k_1/k_3)^2$ in the isotropic case, where the two components make independent contributions (Gulyaev *et al.* 1989), and by a factor of k_1/k_3 in the general axisymmetric case, which involves a cross-product term that drops out in the isotropic case. Then (5.6) shows that the $\bar{u}^{(0)}$ terms are asymptotically small when $R_A \to \infty$ and $\bar{x}$ is in the downstream region where the LUBR equations apply. We therefore neglect these terms and introduce the rescaled variable

$$\tilde{u}\left(\tfrac{1}{2}k_3^2\delta^2, \eta; k_2/k_3, \kappa\right) \equiv \kappa^2 \bar{u}\left(\bar{x}, \eta; \kappa_2, \kappa\right), \tag{6.10}$$

where

$$\delta = \left(2x/R_A\right)^{1/2}, \tag{6.11}$$

along with (6.3) and (6.5) into (6.2) to obtain

$$R_{11}(\tau, \varsigma) = R_A^2 \iiint_{-\infty}^{\infty} \frac{\Phi_t(k_1, k_\perp)}{k_3^2} \left|\tilde{u}\left(\tfrac{1}{2}k_3^2\delta^2, \eta; \frac{k_2}{k_3}, \kappa\right)\right|^2 \mathrm{e}^{\mathrm{i}(k_3\varsigma - k_1\tau)} \mathrm{d}\boldsymbol{k}. \tag{6.12}$$

Our calculations show that $|\tilde{u}|^2$ decays very rapidly as $\kappa \to \infty$, so that the main contribution to the integrand comes from the neighbourhood of $k_1 = 0$. It therefore follows that the mean-square streamwise velocity fluctuation is given by

$$\left\langle u'^2 \right\rangle \equiv R_{11}(0,0) = R_A \int_0^{\infty} \Phi_t(0, k_\perp) K(k_\perp\delta, \eta) k_\perp \mathrm{d}k_\perp, \tag{6.13}$$

in the limit as $R_A \to \infty$ with $\delta = O(1)$, where we have put

$$K(k_\perp\delta, \eta) \equiv 2 \int_0^{\infty} \int_0^{2\pi} \frac{1}{\sin^2\theta} \left|\tilde{u}\left(\tfrac{1}{2}k_\perp^2\delta^2 \sin^2\theta, \eta, \operatorname{cotan}\theta, \frac{\sin^2\theta}{s^{1/2}}\right)\right|^2 \mathrm{d}\theta \, \mathrm{d}s, \tag{6.14}$$

introduced the polar coordinates

$$k_3 = k_\perp \sin\theta, \quad k_2 = k_\perp \cos\theta, \tag{6.15}$$

along with the new integration variable

$$s = k_1 R_A / k_\perp^2 = \sin^2\theta / \kappa^2, \tag{6.16}$$

and used the relation $\bar{u}(-\bar{x}, \eta, \mathrm{i}\kappa_2, \mathrm{i}\kappa) = \bar{u}^*(\bar{x}, \eta, \kappa_2, \kappa)$, which follows from the governing equations and boundary conditions, for the $k_1 < 0$ components.

These results show that only the transverse spectral function, Φ_t, of the upstream turbulence is of direct relevance to the generation and growth of Klebanoff-type disturbances in the boundary layer, as opposed to the longitudinal spectrum function which is most often documented in the experiments. The former function can be determined from measurements of the transverse correlation function

$$R_{\infty\perp}(\xi - \tau, r_\perp) = \left\langle u_\perp(x - t, y, z) u_\perp(x' - t', y', z') \right\rangle, \tag{6.17}$$

where $u_\perp = (u_2^2 + u_3^2)^{1/2}$, $\xi = x' - x$, $\tau = t' - t$, and $r_\perp = ((y' - y)^2 + (z' - z)^2)^{1/2}$, by taking the Hankel transformation of its longitudinal Fourier transform

$$\Phi_t(k_1, k_\perp) = 2 \int_0^{\infty} r_\perp \int_{-\infty}^{\infty} R_{\infty\perp}(\xi - \tau, r_\perp) \mathrm{e}^{\mathrm{i}(\xi - \tau)k_1} \mathrm{d}(\xi - \tau) J_0(r_\perp k_\perp) \, \mathrm{d}r_\perp, \tag{6.18}$$

where J_0 denotes the Bessel function of the first kind in the usual notation.

As far as we know, no such measurements have been made, so the form of this function is still unknown and may differ considerably from one experiment to another. Moreover, the present results show that the velocity fluctuations in the

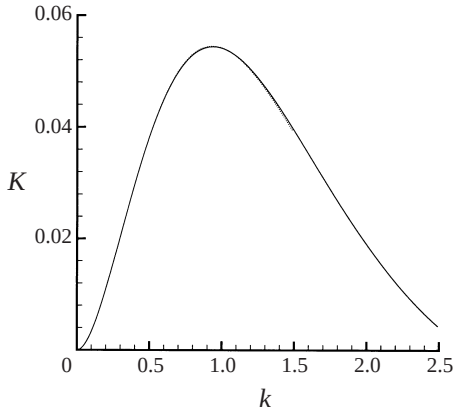

FIGURE 8. Plot of the kernel function K computed from the LUBR solutions (dotted) and the curve fit (7.1) (solid).

boundary layer are determined only by the low-frequency portion of Φ_t, which is the part of the spectrum that is likely to be highly anisotropic (Batchelor 1956, p. 91) – retaining a history of the upstream screens or grid. The low-frequency components of the turbulence should therefore possess a relatively high degree of periodicity in the transverse direction. We will make use of these insights in the next section where the LUBR results are compared with experimental data.

7. Numerical results and comparisons with experimental data

Numerical computations of individual Fourier-component solutions of the LUBR equations were carried out over a broad range of scaled transverse wavenumbers, κ_2 and κ, in order to calculate the mean square of the streamwise velocity fluctuations in the boundary layer. These solutions enter into the expression for the mean-square velocity fluctuation via the kernel function $K(k_\perp\delta, \eta)$, defined by (6.14), which, at a fixed transverse location in the boundary layer, is a function of a single independent variable. The integral in (6.14) was evaluated using the individual Fourier component solutions at fixed $\eta = 1.64$ (which closely corresponds to the peak location of the streamwise velocity fluctuations). The result is shown in figure 8 along with a least-squares fit to the simple functions

$$K(k_*) = k_*^2[-0.03\,\mathrm{e}^{-k_*} + 0.52\,\mathrm{e}^{-2k_*} - 0.08\,\mathrm{e}^{-3k_*}]. \tag{7.1}$$

Equations (7.1) and (6.13) are used to calculate the peak level of the mean-square streamwise velocity fluctuation within the boundary layer in the following computations and comparisons.

Comparisons are made with recent unpublished data of Dr J. M. Kendall (personal communication) and with data of Roach & Brierley (1992) and Westin *et al.* (1994). In the latter two experiments, the investigators attempted to make the incident turbulent flow as isotropic as possible. However, it is very difficult to control the low-frequency component of the spectrum that actually enters the boundary layer to produce the Klebanoff modes. Watmuff (1997) was able to reduce the peak r.m.s. velocity in the boundary layer by as much as 50% by re-ordering the screens upstream of his test section according to the quality of their spanwise uniformity. This suggests that even relatively minor changes in the low-frequency spectral characteristics of the free-

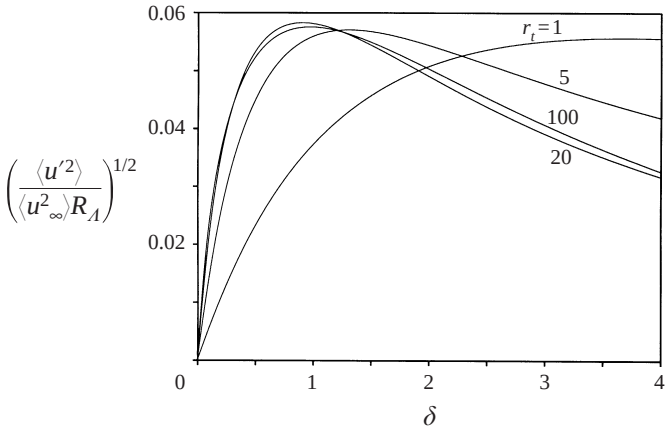

FIGURE 9. Normalized root mean square of the streamwise velocity fluctuations in the boundary layer for isotropic free-stream turbulence at various turbulent Reynolds numbers.

stream turbulence can produce large differences in the r.m.s. velocity in the boundary layer. The inevitable deviations from pure isotropy that occur at low frequencies in any experiment may therefore have an important effect on the velocity fluctuations in the boundary layer. Making use of (7.1) in (6.13) provides a simple and quick method of assessing the effect of various free-stream turbulence spectra on the boundary-layer disturbances.

Figure 9 shows numerical results for the normalized r.m.s. of the streamwise velocity fluctuations, $(\langle u'^2\rangle/\langle u^2_\infty\rangle R_\Lambda)^{1/2}$, plotted vs. δ at $\eta = 1.64$. Here $\langle u^2_\infty\rangle$ denotes the scaled mean-square streamwise velocity fluctuation in the free stream. The free-stream turbulence is assumed to be isotropic with a one-dimensional spectrum given by (Gulyaev *et al.* 1989)

$$E_1(k) = \frac{2\langle u^2_\infty\rangle}{\pi}\frac{\mathrm{e}^{-6.7k/r_t^{3/4}}}{1 + b(2k)^{5/3}}, \tag{7.2}$$

where $b = 1.35/(1 + 35/(2r_t)^{3/4})$, with our normalization. For isotropic turbulence, the normalized r.m.s. streamwise velocity fluctuation depends on the single parameter r_t, which enters only through the one-dimensional spectrum.

Notice that the normalized r.m.s. velocity fluctuation initially increases linearly with δ, which corresponds to the result obtained by using solutions of the linearized boundary-layer equations in place of the boundary-region solutions. However, the spanwise ellipticity effects quickly cause the growth to decrease below the linear boundary-layer results, with the r.m.s. velocity fluctuations reaching a peak and then decreasing with further increase of δ. This is because, even for small δ, the boundary-region solutions selected by the free-stream spectrum do not correspond to small values of κ and κ_2. All the curves reach approximately the same peak level, but those at larger turbulent Reynolds numbers have greater initial slopes and peak at smaller values of δ.

These results suggest that the streamwise velocity fluctuations in the boundary layer can only achieve amplitudes that are three or four times the free-stream level at R_Λ values on the order of a few thousand, which are typical of the recent experiments. However, the experimentally measured boundary-layer fluctuation levels can be several times higher than this. An explanation of this discrepancy is given in

the next subsections, where the linear theory is compared with the experimental data sets alluded to above.

7.1. *Data of Kendall*

Dr J. M. Kendall (personal communication) measured the broadband and band-passed filtered streamwise velocity r.m.s. profiles in the boundary layer over a flat-plate model with elliptical leading edge. The transverse free-stream turbulence level was 0.26%, the free-stream velocity was 11.6 m s^{-1}, and the transverse integral scale near the leading edge (estimated from the lateral correlation of the streamwise velocity fluctuations, Kendall 1990) was 9 mm for this data set, which yields a value for the turbulent Reynolds number, r_t, of about 18. Measurements were taken at streamwise locations corresponding to $\epsilon x^*/\Lambda$ values of between 0.05 and 0.32. The relatively small values of r_t and $\epsilon x^*/\Lambda$ make this experiment one of the best candidates for comparison with linear theory. However, the turbulence was generated upstream of a rather severe (9:1) contraction in this experiment, making the test section turbulence highly anisotropic. This is clearly seen in figure 13 of Kendall (1998), which shows that the transverse velocity fluctuations are roughly five times the level of the longitudinal fluctuations at low frequencies. Since (6.13) shows that only the low-frequency portion of the transverse free-stream spectrum affects the Klebanoff modes, we would not expect the isotropic turbulence model to be in good agreement with the data, which indeed turns out to be the case.

Since, as noted at the end of the previous section, the low-frequency components of the turbulence can be expected to exhibit significant spanwise periodicity, we represent the low-frequency portion of the turbulence spectrum by a class of functions that are potentially more concentrated around a particular transverse wavenumber than the corresponding isotropic spectrum; namely,

$$\Phi_t(0,k_\perp) = \frac{C\langle u_\infty^2\rangle}{\pi^2} k_\perp^2 \mathrm{e}^{-(k_\perp-\bar{k}_\perp)^2/\Delta}, \tag{7.3}$$

where $\bar{k}_\perp$ and Δ are selected to control the position and width of the spectral peak in the crossflow wavenumber, and the constant C is chosen to satisfy (6.9) at $k_1 = 0$.

It follows from the definition of the one-dimensional spectrum that

$$E_t(0) = \frac{2A_1\langle u_\infty^2\rangle}{\pi}, \tag{7.4}$$

where

$$A_1 = \frac{\langle v_\infty^2\rangle}{\langle u_\infty^2\rangle} L_{31}, \tag{7.5}$$

$\langle v_\infty^2\rangle$ is the scaled mean-square transverse velocity fluctuation in the free stream, L_{31} is the integral scale (normalized by Λ) obtained from the time-delayed transverse velocity correlation, and $A_1 = 1$ for isotropic turbulence. We used figure 13 of Kendall (1998) to estimate the numerical value of $E_t(0)$.

Figure 10 shows a comparison of the normalized r.m.s. streamwise velocity computed using (7.3) with $\bar{k}_\perp = -7.0, \Delta = 4$, which puts the peak of the spectral function at $k_\perp = 1.0$, and $A_1 = 140$. Figure 10(*a*) shows that the overall r.m.s. velocity is slightly underpredicted with the chosen values for these quantities, but the lowest frequency band of the filtered data is in very good agreement with the theory (figure 10*b*). While the theoretical curves for the next two frequency bands drop off more rapidly with δ than the data (figure 10*c, d*), an increasing amount of the fluctuation energy moves

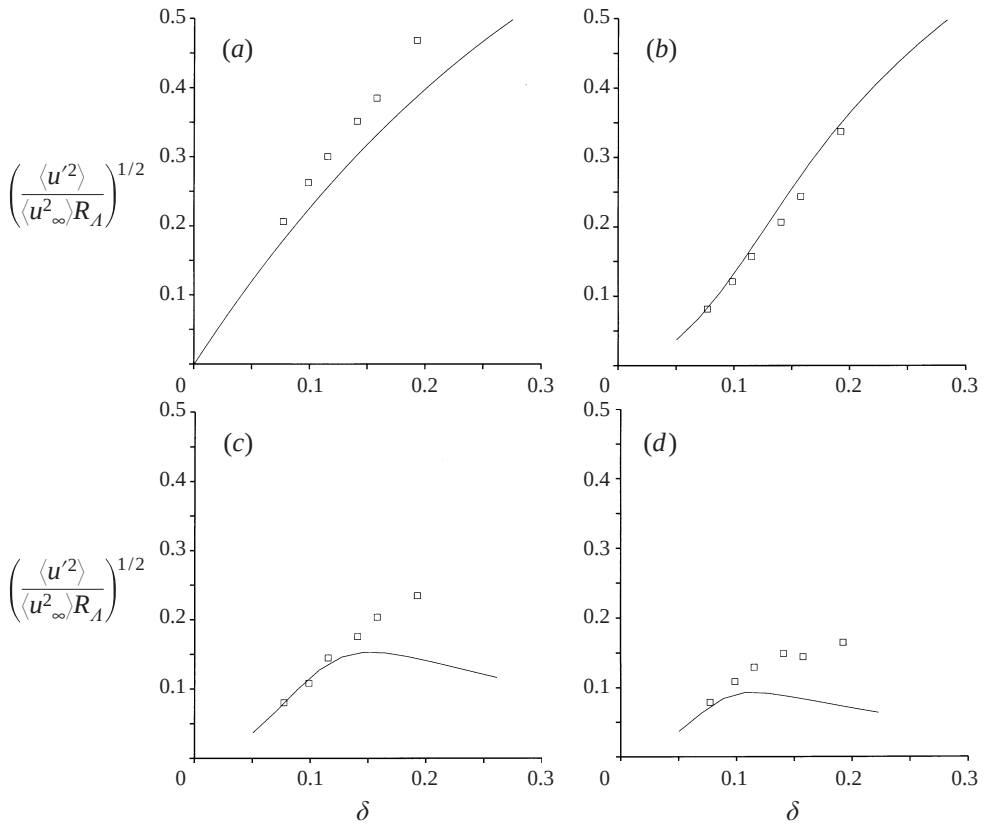

FIGURE 10. Comparison of theoretical results with experimental data of Kendall. (*a*) Broadband r.m.s., (*b*) Band 1: 0–4Hz, (*c*) Band 2: 4–8 Hz, (*d*) Band 3: 8–12 Hz.

into the first band as δ increases, so that the theoretical curve remains fairly close to the broadband experimental results. In fact, Kendall's data shows that about 50% of the energy in the longitudinal velocity fluctuations is in the first band at the last measurement station. The deviation in the higher frequency bands may be due to nonlinear effects, which will be discussed further in the next two subsections. However, it should also be kept in mind that the high-frequency part of the solution will be more affected by streamwise ellipticity effects – neglected in the present analysis – than the low-frequency part.

7.2. *Data of Westin et al.*

Westin *et al.* (1994) conducted experiments at free-stream turbulence levels (based on the streamwise velocity fluctuations) of 1.35% and 1.5%. The ratio of the transverse to streamwise velocity fluctuations was approximately 0.9 in the vicinity of the leading edge. Westin *et al.* (1994) estimated the transverse integral scale of their free-stream turbulence to be between 7 and 10 mm. In the following comparisons we use a value of 8 mm. The corresponding values of R_Λ and r_t are given in the caption of figure 11.

The scaled streamwise distance $\epsilon x^*/\Lambda$ of the measurement points varied between 0.2 and 2.0. This suggests that linear theory may be applicable to the data points closest to the leading edge, even though the turbulent Reynolds number is not particularly small in this experiment, but that further downstream, nonlinear effects

cannot be ignored. In fact, Westin *et al.* (1994) report observing turbulent spots near their last measurement station at the higher turbulence level, and these must certainly be preceded by nonlinear effects.

As pointed out in the Introduction, solutions to the steady nonlinear boundary-layer equations (Goldstein & Leib 1993) and the steady nonlinear boundary-region equations (Wundrow & Goldstein 1998) show that nonlinear interactions in the boundary layer lead to a kind of spanwise focusing effect which can be interpreted as the production of small spanwise length scales. Figure 12 of Westin *et al.* (1994), as well as the data of Kendall, shows that the amplification of the Klebanoff modes is accompanied by a transfer of energy into very low frequencies. It might therefore be expected that the Klebanoff modes behave in a more or less quasi-steady manner once nonlinear effects come into play, and that the main effect of the nonlinearity is to enhance smaller transverse-length-scale components.

We therefore attempt to model the nonlinear effects within the context of linear theory by shifting the peak of the free-stream turbulence spectrum to larger transverse wave numbers as the disturbance amplitude in the boundary layer increases, in order to reflect the increasing prevalence of smaller spanwise scales with increased amplitude. To this end, we used the spectral form (7.3) and allowed the spectral peak location to increase linearly with the maximum r.m.s. streamwise velocity fluctuation in the boundary layer

$$k_\perp^{(P)} = k_\perp^0 + \alpha_1 \varepsilon u', \tag{7.6}$$

where $k_\perp^0$ and α_1 are constants which, along with A_1, were chosen to achieve the best fit with the data.

Nonlinearity can, of course, also become important in the free stream – in which case it would no longer be possible to represent the velocity fluctuations by (5.7) and (5.11) in this region. It might be expected that the boundary-layer nonlinearity is the more important because, as the experiments show, the Klebanoff mode amplitudes are considerably larger than those of the free-stream velocity fluctuations. However, the smaller streamwise length scales of free-stream fluctuations could cause the nonlinear Reynolds stress terms to be larger in the free stream than in the boundary layer. In fact, recent nonlinear computations of the flow in region IV (Wundrow & Goldstein 1998) suggest that nonlinearly in the free stream can be quite significant. Since nonlinear effects are known to produce smaller length scales in almost all turbulent flows (the cascade effect), however, it is possible that (7.6) could account for the free-stream nonlinearity as well.

Figure 11 shows the results of the corresponding calculations along with those based on the linear, isotropic model, which are shown as the dashed curves. These latter predict the initial growth rate fairly accurately, but the strong spanwise ellipticity effects quickly cause the growth to diminish, and the curves reach a more or less constant level. While this level is of about the right order of magnitude, it is well below the experimental levels. The discrepancy is greatest at the larger turbulent Reynolds number and increases with downstream distance – consistent with expectations for the linear theory.

The solid curves in the figure were computed from (7.3) and (7.6) with values for the parameters given in the caption. These results show that agreement with the data is greatly improved when low-frequency anisotropy and nonlinear effects are included. As expected, the A_1 values required to fit these data sets are much closer to the isotropic value than the A_1 value used in the Kendall comparison.

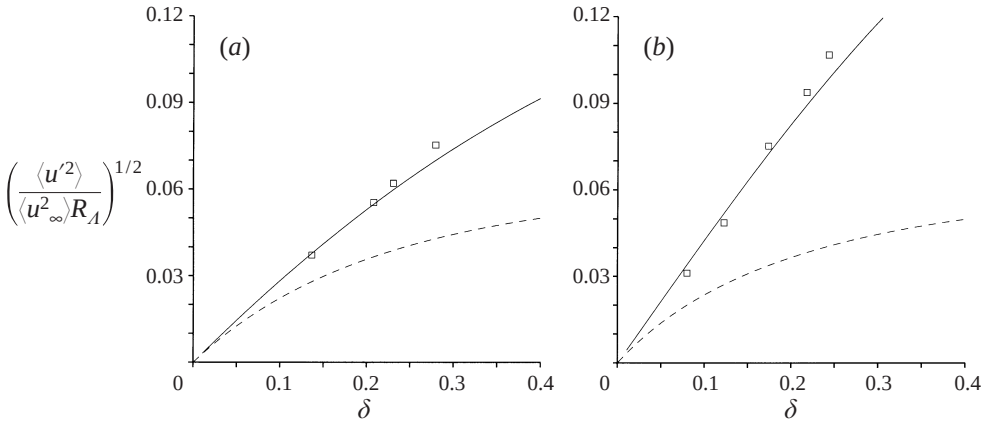

FIGURE 11. Comparison of theoretical results with experimental data of Westin *et al.* (1994). Dashed curves are for isotropic turbulence, solid curves for anisotropic form (7.3) with (7.6) and $k_\perp^0 = 0.6, \Delta = 10, \alpha_1 = 1.3$. (*a*) $Tu = 1.35\,\%, R_A = 2120, r_t = 26, A_1 = 5$, (*b*) $Tu = 1.5\,\%, R_A = 4240, r_t = 58, A_1 = 10$.

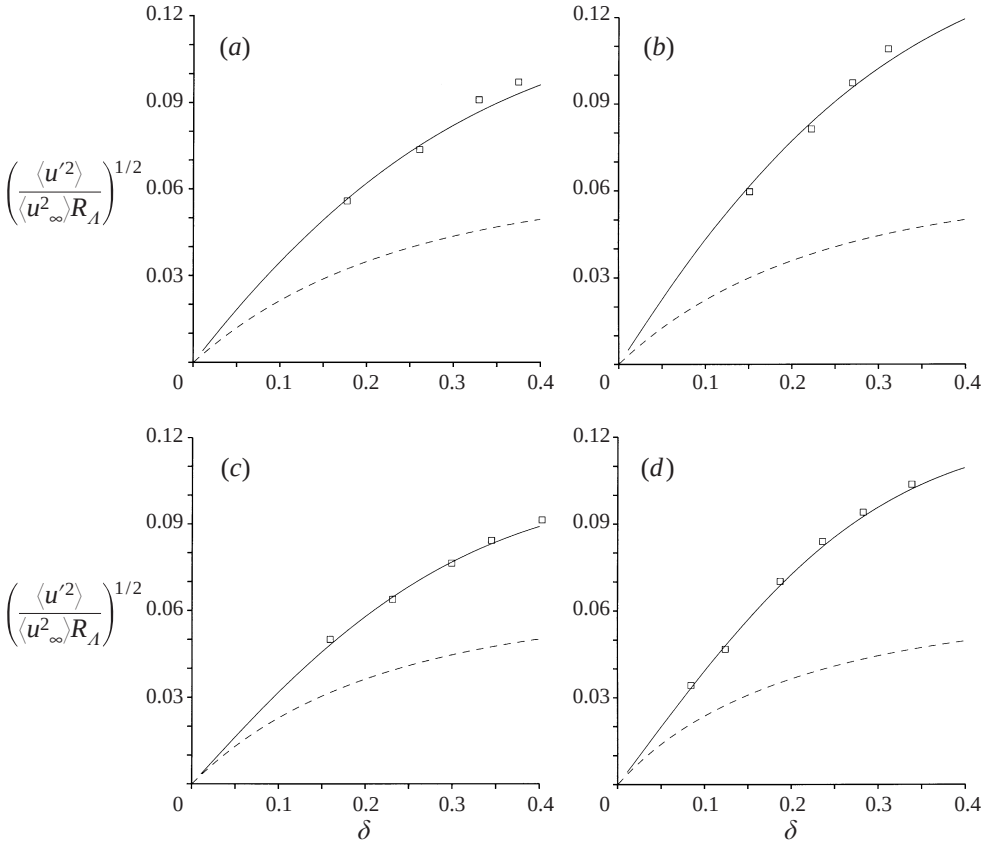

FIGURE 12. Comparison of theoretical results with experimental data of Roach & Brierley (1992). Dashed curves are for isotropic turbulence, solid curves for anisotropic form (7.3) with (7.6) and $k_\perp^0 = 1.0, \Delta = 10, \alpha_1 = 1.3$. (*a*) SMRLO, $Tu = 0.8\,\%, R_A = 2400, r_t = 19, A_1 = 3$, (*b*) SMRHI, $Tu = 0.8\,\%, R_A = 3200, r_t = 26, A_1 = 4.5$, (*c*) PRLO, $Tu = 3.0\,\%, R_A = 1200, r_t = 36, A_1 = 2.3$, (*d*) PRHI, $Tu = 3.0\%, R_A = 2100, r_t = 63, A_1 = 3.2$.

7.3. *Data of Roach & Brierley*

Roach & Brierley (1992) carried out experiments over a fairly broad range of free-stream turbulence levels with a variety of turbulence-generating grids. We compare our results with data from four of their runs – the others having either no organizing grid or extremely high turbulence levels. Roach (1987) presents detailed measurements of the intensities and scales of the turbulence generated by the grids used in the Roach & Brierley (1992) experiments and suggests empirical formulas for their description. The upstream turbulence was quite isotropic in these experiments, with the streamwise and transverse fluctuation levels being nearly identical in the test section. The values of the physical parameters for the four runs considered are given in the caption of figure 12.

The data were taken at scaled distances $\epsilon x^*/\Lambda$ that varied from 0.2 to 8.5. These data then, like the Westin *et al.* (1994) data, encompass a region where we would expect the linear theory to apply, but also extend well into the nonlinear regime.

Figure 12 shows the comparisons of the present results with the Roach & Brierley (1992) data. As in the Westin *et al.* (1994) case, the linear isotropic curves (dashed) begin with about the right growth rate, with the greatest deviations being at large δ and r_t. The solid curves are computed from (7.3) and (7.6) with parameter values indicated in the caption. The values for A_1 are somewhat closer to the isotropic value than those used for the Westin *et al.* (1994) data, consistent with the relative degree of isotropy reported for these experiments. Again, larger values of A_1 are required at the higher turbulence levels for a given grid – possibly indicating a greater degree of low-frequency anisotropy at the higher free-stream velocities.

These results suggest that low-frequency anisotropy plays an important role in the generation of Klebanoff modes and that nonlinear effects strongly influence their subsequent growth at the higher turbulent Reynolds numbers.

8. Discussion

We have carried out a systematic linear analysis of the effects of vortical free-stream disturbances on a laminar flat-plate boundary layer. The upstream distortion was decomposed into its various Fourier components. The analysis describes the resulting downstream evolution of the flow, first through an unsteady boundary-layer region and then into a region where spanwise ellipticity effects are important. The flow in the latter region is governed by the linearized unsteady boundary-region (LUBR) equations, which were solved numerically subject to upstream and far-field boundary conditions derived from strict asymptotic matching of the solutions in the various regions shown in figure 1. The spanwise ellipticity effects are surprisingly strong and very quickly influence the growth of the disturbances. The linearized approximation allows us to superpose the individual Fourier-component solutions to the LUBR equations and thereby calculate the r.m.s. streamwise velocity fluctuations in the boundary layer due to a broadband external turbulent flow. The analysis shows that it is the low-frequency transverse velocity fluctuations in the free stream that are primarily responsible for the generation of Klebanoff modes. Results were obtained for isotropic turbulence and for axisymmetric turbulence with low-frequency anisotropy.

Comparison of the theoretical calculations with recent experimental data shows that the disturbances produced by the linear mechanism described above closely resemble the behaviour actually observed for Klebanoff modes. The theoretical results for

isotropic turbulence predict the initial linear growth with boundary-layer thickness but, due to the strong pressure coupling effects in the boundary-region equations, the amplitudes do not reach the levels found in the experiments. Calculations using an anisotropic model for the free-stream turbulence suggests that low-frequency anisotropic effects could be a significant factor in explaining the discrepancy.

Detailed comparisons have been made with three different experiments over a range of flow conditions. The linear theory was compared with the data of Kendall, which is one of the lowest turbulent-Reynolds-number data sets available. A low-frequency anisotropic model was used for the free-stream spectrum function. Good agreement was obtained with the lowest frequency band of his band-passed filtered data. However, there was an increasing discrepancy with downstream distance from the leading edge in the higher frequency bands, which may be due to nonlinear effects. Since the energy content of the low-frequency band increases with increased Klebanoff-mode amplitude, the theoretical broadband r.m.s. curve also remains quite close to the data, which suggests that the nonlinear effects may enter in a more or less quasi-steady manner. It is worth noting that numerical solutions of the nonlinear, steady boundary-region equations show that nonlinear effects produce significant local changes in the disturbance velocity profiles, but have only a weak effect on the spanwise-averaged r.m.s. streamwise velocity fluctuation (Leib *et al.* 1999). The theoretical curve for the lowest frequency band in figure 10 might therefore be relatively unaffected by nonlinearity, which may however influence the higher frequency bands.

The higher turbulent Reynolds numbers in the Roach & Brierley (1992) and Westin *et al.* (1994) experiments may exceed the range of applicability of the purely linear theory, and the observation of turbulent spots by Westin *et al.* (1994) suggests that nonlinear effects are at work there. However, the linear theory has many advantages which we would like to retain if at all possible. We therefore attempted to modify it to account for the dominant nonlinear effect, namely enhancement of the small-transverse-length-scale components (Wundrow & Goldstein 1998), by allowing the relative weighting of the large-transverse-wavenumber components of the free-stream spectrum function to increase with increasing boundary-layer disturbance amplitude. We have shown that the predictions of this modified linear theory are in very good agreement with the data of Roach & Brierley (1992) and Westin *et al.* (1994).

Westin *et al.* (1994) collected much of the available experimental data on a single plot of $(\langle u'^2\rangle/\langle u_\infty^2\rangle)^{1/2}$ vs. boundary-layer thickness. They showed that, with some notable exceptions, the data tend to follow a straight line, but that the slope of the line differs from one experiment to another. The Kendall data shown in figure 10 would have a much larger slope than the other data sets if it were included in this plot. In fact, Kendall's Klebanoff-mode amplitudes were nearly as large as those found by Westin *et al.* (1994), even though Kendall's free-stream streamwise velocity fluctuation level was much smaller than Westin *et al.*'s. The present analysis shows that this is because the Klebanoff modes are driven by the low-frequency transverse velocity fluctuations and not by the streamwise velocity fluctuations, while figure 13 of Kendall (1998) shows that the low-frequency limit of the transverse velocity fluctuations is much larger than the streamwise velocity fluctuation in his experiment, due to a relatively severe contraction upstream of the test section. The free-stream turbulence in the Westin *et al.* (1994) experiment was, on the other hand, fairly isotropic.

Bertolotti (1997) carried out an *ad hoc* analysis of the problem considered in this paper by using the parabolic stability equations. Results from linear calculations

with a single, steady, free-stream mode were compared with the data of Westin *et al.* (1994), and agreement was obtained by selecting the modal amplitude to produce the best results. Bertolotti (1997) also made comparisons with recent, unpublished, data of Kendall. Of particular interest is the comparison with filtered r.m.s. data for various frequency bands. The computations qualitatively predict the large amplification of the low-frequency components that was observed in the experiment, but generally underpredict the actual amplitudes, with the agreement being worse at large downstream distances and higher frequencies.

Our analysis differs from that of Bertolotti (1997) in a number of important aspects. First, we have derived our governing equations and boundary conditions in a rational way from the Navier–Stokes equations. Secondly, we have made use of the major attraction of the linear theory, namely its superposition feature, to combine the individual Fourier component solutions to obtain results corresponding to an actual broadband turbulent flow. Moreover, our results suggest that nonlinear effects play an important role in the development of Klebanoff modes in many of the most important experiments. This effect increases with increasing downstream distance from the leading edge and possibly with increasing frequency.

As already mentioned, the analysis is restricted to what appears to be the dominant generation and amplification mechanism of low-frequency disturbances in the boundary layer, namely the linear amplification of crossflow-driven disturbances in the boundary layer on an infinitely-thin flat plate. There are numerous other effects present in the experiments which might potentially contribute to the amplification of the disturbances.

Our calculations of u r.m.s. include only the contribution from the three-dimensional component $\bar{u}$. The two-dimensional $\bar{u}^{(0)}$ component makes an independent, but asymptotically smaller, contribution to the r.m.s. velocity fluctuation for isotropic free-stream turbulence. However, there is an interaction term involving the $\bar{u}$ and $\bar{u}_0$ components in the general axisymmetric case which, while still asymptotically small compared with the $\bar{u}$ contribution, is larger than the terms neglected in the isotropic case.

Kendall (1991) and Watmuff (1997) found that changing the leading-edge bluntness of their plates had very little effect on the amplitude or spanwise spacing of the disturbances in the boundary layer. However, stretching of vortex lines initially normal to the plate by a relatively blunt leading edge produces a streamwise vorticity (crossflow) which is then imposed on the boundary-layer flow (Goldstein *et al.* 1992; Goldstein & Wundrow 1998). This mechanism leads to augmentation of the disturbance amplification relative to that of an infinitely-thin plate. However, these experiments involved a relatively large contraction which greatly reduced the streamwise velocity and, therefore, the normal vorticity relative to the spanwise velocity, especially in the low-frequency part of the spectrum that actually generates the Klebanoff modes (as can be seen from figure 13 of Kendall 1998). It is worth noting that the leading-edge bluntness effects were not investigated in the experiments (such as those of Roach & Brierley 1992 and Westin *et al.* 1994) where the turbulence grid was placed downstream of the contraction.

Additional theoretical and experimental work is required before a full understanding of the Klebanoff mode generation and growth mechanisms is in hand. On the theoretical side, the additional effects discussed above could each be analysed separately, and then superposed when linear theory can be used. However, it is probably more important to incorporate a better description of the nonlinear effects. A major difficulty which arises from this is that the free-stream modes can no longer be

superposed to represent the external turbulent flow. A full simulation of the problem, including the free-stream turbulence, is impractical with current computational capabilities, so that some type of modelling of the flow is required. Unfortunately, this is not yet completely developed, but perhaps the quasi-linear theory described above is a good start in this direction.

On the experimental side, our analysis suggests that important information could be obtained from detailed measurements of the low-frequency portion of the free-stream turbulence spectrum and, in particular, the relative degree of anisotropy therein. In addition, measurements of the transverse correlation function $R_{\infty\perp}$ of the free-stream turbulence would provide the input needed to compute the boundary-layer u r.m.s. in our axisymmetric model. This would allow a more definitive test of the present linear theory and might suggest further lines of research to develop a fuller understanding of this phenomena.

The exact role played by the Klebanoff modes in the laminar–turbulent transition process is still not completely clear. They can reach very large amplitudes in the boundary layer before transition occurs, whereas Tollmien–Schlichting waves provoke transition at much lower levels. Experiments by Boiko *et al.* (1994) show that sufficiently high levels of free-stream turbulence can produce significant transfer of energy between frequencies within the unstable bands for TS waves. It is therefore possible that the Klebanoff modes primarily influence transition by modifying the base flow, which, among other things, causes a broadening of the frequency band over which the TS waves can grow. A stability analysis of such a base flow, i.e. the Blasius profile with Klebanoff modes superposed, could shed additional light on this issue. Wundrow & Goldstein (1994), Wundrow (1996), Goldstein & Wundrow (1995) and Wundrow & Goldstein (1998) have already made some progress along these lines.

Another possibility is that large-amplitude Klebanoff modes can generate turbulent spots directly by producing a local separation of the flow. This has been investigated by Wundrow & Goldstein (1998).

The authors would like to thank Dr James Kendall for supplying his unpublished experimental data and Professor Eli Reshotko for his encouragement and helpful comments.

Appendix A. Edge layer solution for asymptotic LUBL equations

Equation (4.21) suggests that the appropriate transverse coordinate in the edge layer is given by

$$\bar{\eta} \equiv \eta - \beta = \eta_0 + \delta_0 \hat{\eta}, \tag{A 1}$$

where η_0 is determined by

$$2\bar{x}A = \eta_0^3 \, \mathrm{e}^{\eta_0^2/2}, \tag{A 2}$$

and $\delta_0(\bar{x})\delta\Lambda$ is the edge layer thickness. Then the mean velocity will exhibit an order-one variation across the edge layer if we put

$$\delta_0 \, \eta_0 = 1. \tag{A 3}$$

Substituting these into the LUBL equations, (4.5) and (4.11), shows that

$$\{\bar{u}, \bar{v}, \bar{w}\} = \{\bar{u}_e, \delta_0 \, \bar{v}_e, \bar{w}_e\} \, \mathrm{e}^{\mathrm{i}\bar{x}}, \tag{A 4}$$

are determined by

$$(\mathrm{i}\bar{u}_e - \bar{v}_e)\,\mathrm{e}^{-\hat{\eta}} + \frac{\partial \bar{u}_e}{\partial \hat{\eta}} + \frac{\partial^2 \bar{u}_e}{\partial \hat{\eta}^2} = 0, \tag{A 5}$$

$$\mathrm{i}\bar{w}_e\,\mathrm{e}^{-\hat{\eta}} + \frac{\partial \bar{w}_e}{\partial \hat{\eta}} + \frac{\partial^2 \bar{w}_e}{\partial \hat{\eta}^2} = 0, \tag{A 6}$$

$$\mathrm{i}\bar{u}_e + \frac{\partial \bar{v}_e}{\partial \hat{\eta}} + \bar{w}_e = 0, \tag{A 7}$$

subject to the boundary conditions

$$\bar{u}_e \to 0, \bar{w}_e \to 1 \quad \text{as} \quad \hat{\eta} \to \infty, \tag{A 8}$$

and that $\bar{w}_e\,\mathrm{e}^{\mathrm{i}\bar{x}}$ match onto (4.17) as $\eta \to -\infty$, with a similar condition for $\bar{u}_e$. As suggested by Gulyaev *et al.* (1989), (A 6) can easily be solved in terms of Hankel functions to obtain

$$\bar{w}_e = -\mathrm{i}^{-1/2}\pi \mathrm{e}^{-\hat{\eta}/2} H_1^{(1)}(2\mathrm{i}^{1/2}\mathrm{e}^{-\hat{\eta}/2}), \tag{A 9}$$

which clearly satisfies the outer-edge boundary condition (A 8), while the large argument expansion for $H_1^{(1)}$ shows that

$$\bar{w}_e \to (\pi)^{1/2}\mathrm{e}^{-\mathrm{i}\pi/8}\mathrm{e}^{-\hat{\eta}/4}\mathrm{e}^{-2\mathrm{i}^{1/2}\mathrm{e}^{-\hat{\eta}/2}} \quad \text{as} \quad \hat{\eta} \to -\infty, \tag{A 10}$$

which, in view of (A 1)–(A 4) and (4.17)–(4.19), will match onto (4.17) if we take

$$c_0 = (-\mathrm{i}\pi A)^{1/2}\,(2\bar{x})^{1/4}\mathrm{e}^{-H_\infty + \mathrm{i}\pi/8}, \tag{A 11}$$

where $H_\infty \equiv \lim_{\bar{\eta}\to\infty}(H + \frac{1}{4}\bar{\eta}^2 + \ln\bar{\eta})$.

Appendix B. Power series solution for the LUBR equations

The equations for the first two terms of the power series (5.24) are

$$U_0'' + FU_0' + (\eta F'' - 2F')U_0 - F''V_0 = 0, \tag{B 1}$$

$$P_0' = 0, \tag{B 2}$$

$$W_0'' + FW_0 = 0, \tag{B 3}$$

$$2U_0 - \eta U_0' + V_0' + W_0 = 0, \tag{B 4}$$

and

$$U_1'' + FU_1' + (\eta F'' - 3F')U_1 - F''V_1 = 0, \tag{B 5}$$

$$P_1' = V_0'' + FV_0' - (\eta F')'V_0 + [\eta(\eta F')' - F]U_0, \tag{B 6}$$

$$W_1'' + FW_1' - F'W_1 = -\kappa^2 P_0, \tag{B 7}$$

$$3U_1 - \eta U_1' + V_1' + W_1 = 0. \tag{B 8}$$

Equations (B 1)–(B 8) must be solved subject to the no-slip condition at $\eta = 0$. The boundary conditions at $\eta \to \infty$ are obtained by matching with the limit of (5.20)–(5.23) as $\bar{x} \to 0$ with $\eta = O(1)$. Finally, the boundary-region solution must match onto the low-frequency, boundary-layer solution as $\bar{x} \to 0$ with $\eta = O(1)$.

Putting $y^{(0)} = (2\bar{x})^{1/2}\,\bar{\eta}$ in (5.21) and (5.22) and letting $\bar{x} \to 0$ with $\eta = O(1)$ gives

$$\bar{v} \to -\bar{\eta} - \frac{\mathrm{i}}{2}(2\bar{x})^{1/2}(\kappa_2 + \mathrm{i}\,|\kappa|)[\bar{\eta}^2 + 1] + \frac{|\kappa|}{(2\bar{x})^{1/2}}[1 - |\kappa|\,(2\bar{x})^{1/2}\bar{\eta}] \int_0^{\bar{x}} g(\check{x})\mathrm{e}^{-\mathrm{i}\check{x}}\mathrm{d}\check{x} + \cdots, \tag{B 9}$$

and

$$\bar{w} \to 1 + (2\bar{x})^{1/2}\mathrm{i}\left(\kappa_2 + \mathrm{i}\,|\kappa|\right)\bar{\eta} + \kappa^2 \int_0^{\bar{x}} g(\check{x})\mathrm{e}^{-\mathrm{i}\check{x}}\mathrm{d}\check{x} + \cdots. \tag{B 10}$$

The solution to (B 1), (B 3) and (B 4) is given by the first of (4.13) and matching with (B 9) requires that

$$g(\bar{x}) \to \frac{-3\beta}{4\,|\kappa|}\frac{1}{(2\bar{x})^{1/2}} + g_1 + \cdots \quad \text{as} \quad \bar{x} \to 0, \tag{B 11}$$

where g_1 is a constant. It therefore follows from (5.23) and (B 2) that

$$P_0 = -\frac{3\beta}{4\,|\kappa|}. \tag{B 12}$$

Substituting (B 11) into (B 10), and matching with the power series solution, leads to the boundary condition

$$W_1 \to \mathrm{i}(\kappa_2 + \mathrm{i}\,|\kappa|)\bar{\eta} - \frac{3\beta\,|\kappa|}{4} \quad \text{as} \quad \eta \to \infty, \tag{B 13}$$

for (B 7).

It is clear from (5.20) that $U_1 \to 0$ as $\eta \to \infty$. Using this along with (B 13) in (B 8) shows that

$$V_1 \to \mathrm{i}(\kappa_2 + \mathrm{i}\,|\kappa|)(\tfrac{1}{2}\eta^2 - \beta\eta) + \frac{3\beta\,|\kappa|}{4}\eta + c_1 \quad \text{as} \quad \eta \to \infty, \tag{B 14}$$

where c_1 is a constant determined by the numerical solution (note that no boundary condition may be imposed on V_1 as $\eta \to \infty$).

Matching (B 14) with the $O((2\bar{x})^{1/2})$ terms in (B 9), and using (B 11), shows that

$$g_1 = \frac{2c_1}{|\kappa|} + \frac{3\beta^2}{2} + \mathrm{i}(\kappa_2/\,|\kappa| + \mathrm{i})(\beta^2 + 1). \tag{B 15}$$

Appendix C. The common parts of the composite solutions (5.26) and (5.27)

Equations (5.25)–(5.27) constitute a composite solution for the boundary-region equations which is valid for $\bar{x} \to 0$ with $y^{(0)} = O(1)$. They were obtained by adding (5.24) to (5.20)–(5.23) and subtracting out the common parts. Equations (B 9)–(B 16) show that the appropriate common parts are

$$\bar{v}_c = -\bar{\eta} - \frac{3\beta}{4} + (2\bar{x})^{1/2}\left\{-\frac{\mathrm{i}}{2}(\kappa_2 + \mathrm{i}\,|\kappa|)[\bar{\eta}^2 + 1] + \frac{3\beta\,|\kappa|}{4}\bar{\eta} + \tfrac{1}{2}\,|\kappa|\,g_1\right\}, \tag{C 1}$$

and

$$\bar{w}_c = 1 + (2\bar{x})^{1/2}\left[\mathrm{i}(\kappa_2 + \mathrm{i}\,|\kappa|)\bar{\eta} - \frac{3\beta\,|\kappa|}{4}\right]. \tag{C 2}$$

Appendix D. Axisymmetric turbulence

The general form of the energy spectrum tensor in axisymmetric turbulence is (Batchelor 1946, 1953; Chandrasekhar 1950)

$$\Phi_{ij} = Ak_i k_j + B\delta_{i1}\,\delta_{j1} + C\delta_{ij} + Dk_i\,\delta_{j1} + Ek_j\,\delta_{i1}, \tag{D 1}$$

where A, B, C, D and E are scalar functions of k_1 and $k^2 = k_1^2 + k_2^2 + k_3^2$.

The number of arbitrary functions can be reduced by using incompressibility to show that the spectral tensor can be expressed in terms of two scalar functions (Lindborg 1995)

$$\Phi_{ij} = A\left(k^2\delta_{ij} - k_i k_j\right) + D\left(k_i\,\delta_{j1} + k_j\,\delta_{i1} - \frac{k^2}{k_1}\delta_{i1}\delta_{j1} - k_1\delta_{ij}\right). \tag{D 2}$$

We replace the two scalars A and D with the functions

$$\Phi_1(k_1, k_\perp) = \Phi_{11}, \tag{D 3}$$

and

$$\Phi_t(k_1, k_\perp) = \Phi_{22} + \Phi_{33}, \tag{D 4}$$

which are related to the longitudinal and lateral one-dimensional spectra, $E_1(k_1)$ and $E_t(k_1)$, by (6.7) and (6.8), respectively.

Eliminating A and D from (D 2)–(D 4) yields

$$\begin{aligned}\Phi_{ij} = &\left(\frac{2k_1^2}{k_\perp^4}\Phi_1 - \frac{1}{k_\perp^2}\Phi_t\right)(k_i k_j - k^2\delta_{ij}) \\ &-\frac{k_1}{k_\perp^2}\left[\left(1 + \frac{2k_1^2}{k_\perp^2}\right)\Phi_1 - \Phi_t\right]\left(k_i\,\delta_{j1} + k_j\,\delta_{i1} - \frac{k^2}{k_1}\delta_{i1}\delta_{j1} - k_1\delta_{ij}\right).\end{aligned} \tag{D 5}$$

REFERENCES

Arnal, D. & Juillen, J. C. 1978 Contribution experimentale l'etude de la receptivite d'une couche limite laminare, a la turbulence de l'ecoulement general. *ONERA Rapport Technique* No. 1/5018 AYD.

Batchelor, G. K. 1946 The theory of axisymmetric turbulence. *Proc. R. Soc. Lond.* A **186**, 480–502.

Batchelor, G. K. 1953 *The Theory of Homogeneous Turbulence*. Cambridge University Press.

Batchelor, G. K. & Proudman, I. 1954 The effect of rapid distortion of a fluid in turbulent motion. *Q. J. Mech. Appl. Maths* **7**, 83–103.

Bertolotti, F. P. 1997 Response of the Blasius boundary layer to free-stream vorticity. *Phys. Fluids* **9**, 2286–2299.

Blair, M. F. 1992 Boundary-layer transition in accelerating flows with intense freestream turbulence: Part 1 – Disturbances upstream of transition onset. *Trans. ASME: J. Fluids Engng* **114**, 313–321.

Boiko, A. V., Westin, K. J. A., Klingmann, B. G. B., Koslov, V. V. & Alfredsson, P. H. 1994 Experiments in a boundary layer subjected to free stream turbulence. Part 2. The role of TS waves in the transition process. *J. Fluid Mech.* **281**, 219–245.

Brown, S. N. & Stewartson, K. 1973 On the propagation of disturbances in a laminar boundary layer. I. *Proc. Camb. Phil. Soc.* **73**, 493–503.

Cantwell, B. J., Coles, D. E. & Dimotakis, P. E. 1978 Structure and entrainment in the plane of symmetry of a turbulent spot. *J. Fluid Mech.* **87**, 641–672.

Chandrasekhar, S. 1950 The theory of axisymmetric turbulence. *Phil. Trans. R. Soc. Lond.* A **242**, 557–577.

Choudhari, M. 1996 Boundary layer receptivity to three-dimensional unsteady vortical disturbances in free stream. *AIAA Paper* 96-0181 (and *High Technology Inc. Rep.* HTC-95051.)

Crow, S. C. 1966 The spanwise perturbation of two-dimensional boundary layers. *J. Fluid Mech.* **24**, 153–164.

Davis, R. T. & Rubin, S. G. 1980 Non-Navier–Stokes viscous flow computations. *Comput. Fluids* **8**, 101–131.

Dryden, H. L. 1936 Air flow in the boundary layer near a plate. *NACA Rep.* 562.

Goldstein, M. E. 1978 Unsteady vortical and entropic distortions of potential flows round arbitrary obstacles. *J. Fluid Mech.* **89**, 433–468.

Goldstein, M. E. 1983 The evolution of Tollmien–Schlichting waves near a leading edge. *J. Fluid Mech.* **127**, 59–81.

Goldstein, M. E. 1995 The role of nonliner critical layers in boundary layer transition. *Phil. Trans. R. Soc. Lond.* A **352**, 425–447.

Goldstein, M. E. 1997 Response of the pre-transitional laminar boundary layer to free stream turbulence. Otto Laporte Lecture. *Bull. Am. Phys. Soc.* **42**, 2150.

Goldstein, M. E. & Choi, S. W. 1989 Nonlinear evolution of interacting oblique waves on two-dimensional shear layers. *J. Fluid Mech.* **207**, 97–120 (and Corrigendum *J. Fluid Mech.* **216**, 1990, 659).

Goldstein, M. E. & Durbin, P. A. 1980 The effect of finite turbulence spatial scale on the amplification of turbulence by a contracting stream. *J. Fluid Mech.* **98**, 473–508.

Goldstein, M. E. & Leib, S. J. 1993 Three-dimensional boundary layer instability and separation induced by small-amplitude streamwise vorticity in the upstream flow. *J. Fluid Mech.* **246**, 21–41.

Goldstein, M. E., Leib, S. J. & Cowley, S. J. 1992 Distortion of a flat plate boundary layer by free stream vorticity normal to the plate. *J. Fluid Mech.* **237**, 231–260.

Goldstein, M. E. & Wundrow, D. W. 1995 Interaction of oblique instability waves with weak streamwise vortices. *J. Fluid Mech.* **284**, 377–407.

Goldstein, M. E. & Wundrow, D. W. 1998 On the environmental realizability of algebraically growing disturbances and their relation to Klebanoff modes. *Theor. Comput. Fluid Dyn.* **10**, 171–186.

Gulyaev, A. N., Kozlov, V. E., Kuznetson, V. R., Mineev, B. I. & Sekundov, A. N. 1989 Interaction of a laminar boundary layer with external turbulence. *Izv. Akad. Nauk SSSR Mekh. Zhid. Gaza* **6**, 700–710.

Hunt, J. C. R. 1973 A theory of turbulent flow round two-dimensional bluff bodies. *J. Fluid Mech.* **61**, 625–706.

Kemp, N. 1951 The laminar three-dimensional boundary layer and a study of the flow past a side edge. MAcS Thesis, Cornell University.

Kendall, J. M. 1985 Experimental study of disturbances produced in a pre-transitional laminar boundary layer by weak free stream turbulence. *AIAA Paper* 85-1695.

Kendall, J. M. 1990 Boundary layer receptivity to free stream turbulence. *AIAA Paper* 90-1504.

Kendall, J. M. 1991 Studies on laminar boundary layer receptivity to freestream turbulence near a leading edge. In *Boundary Layer Stability and Transition to Turbulence* (ed. D. C. Reda, H. L. Reed & R. Kobayashi). ASME FED, vol. 114, pp. 23–30.

Kendall, J. M. 1998 Experiments on boundary-layer receptivity to freesteam turbulence. *AIAA Paper* 98-0530.

Klebanoff, P. S. 1971 Effect of free-stream turbulence on a laminar boundary layer. *Bull. Am. Phys. Soc.* **16**

Kline, S. J., Reynolds, W. C., Schraub, F. A. & Runstadler, P. W. 1967 The structure of turbulent boundary layers. *J. Fluid Mech.* **30**, 741–773.

Kosorygin, V. S., Polyakov, N. F., Suprun, T. T. & Epik, E. Ya. 1982 Development of perturbations in laminar boundary layer of plate with increased turbulence of external flow. In *Instability of Subsonic and Supersonic Flows.* Siberian Branch USSR Academy of Science, Novosibirsk.

Lam, S. H. & Rott, N. 1960 Theory of linearized time dependent boundry layers. *Cornell Univ. Grad. School of Aero. Engng Rep. AFOSR* TN-60-1100.

Leib, S. J., Wundrow, D. W. & Goldstein, M. E. 1999 Generation and growth of boundary layer disturbances due to free stream turbulence. *AIAA Paper* 99-0408. (in press).

Leventhal, L. & Reshotko, E. 1981 Preliminary experimental study of disturbances in a laminar boundary layer due to distributed surface roughness. *AIAA Paper* 81-1224.

Lighthill, M. J. 1954 The response of laminar skin friction and heat transfer to fluctuations in the stream velocity. *Proc. R. Soc. Lond.* A **224**, 1–23.

LINDBORG, E. 1995 Kinematics of homogeneous axisymmetric turbulence. *J. Fluid Mech.* **302**, 179–201.

ROACH, P. E. 1987 The generation of nearly isotropic turbulence by means of grids. *Intl J. Heat Fluid Flow* **8**, 82–92.

ROACH, P. E. & BRIERLEY, D. H. 1992 The influence of a turbulent free stream on zero pressure gradient transitional boundary layer development. Part I: Test cases T3A and T3B. In *Numerical Simulation of Unsteady Flows and Transition to Turbulence* (ed. O. Pironneau, W. Rodi, I. L. Ryhming, A. M. Saville & T. V. Truong), pp. 319–347. Cambridge University Press.

SCHLICHTING, H. 1955 *Boundary Layer Theory*. McGraw-Hill.

SUDER, K. L., O'BRIEN, J. E. & RESHOTKO, E. 1988 Experimental study of bypass transition in a boundary layer. *NASA Tech Mem.* 100913.

TAYLOR, G. I. 1939 Some recent developments in the study of turbulence. In *Proc. Fifth Intl Congr. for Applied Mechanics* (ed. J. P. Den Hartog & H. Peters), pp. 294–310. Wiley.

VAN DYKE, M. D. 1975 *Perturbation Methods in Fluid Mechanics*. Parabolic.

WESTIN, K. J. A., BOIKO, A. V., KLINGMANN, B. G. B., KOZLOV, V. V. & ALFREDSSON, P. H. 1994 Experiments in a boundary layer subjected to free stream turbulence. Part 1. Boundary layer structure and receptivity. *J. Fluid Mech.* **281**, 193–218.

WATMUFF, J. H. 1997 Detrimental effects of almost immeasurably small free-stream nonuniformities generated by wind tunnel screens. *AIAA Paper* 97-0228.

WUNDROW, D. W. 1996 Linear instability of a uni-directional transversely sheared mean flow. *NASA CR* 198535.

WUNDROW, D. W. & GOLDSTEIN, M. E. 1994 Nonlinear instability of a uni-directional transversely sheared mean flow. *NASA TM* 106779.

WUNDROW, D. W. & GOLDSTEIN, M. E. 1998 Effect on a laminar boundary layer of small-amplitude streamwise vorticity in the upstream flow. Submitted to *J. Fluid Mech.*